# STAR IMAGER FOR NANOSATELLITE APPLICATIONS

ANDREW JOACHIM LOHMANN

A THESIS SUBMITTED TO THE FACULTY OF GRADUATE STUDIES IN PARTIAL FULFILLMENT OF THE REQUIREMENTS FOR THE DEGREE OF MASTER OF SCIENCE

GRADUATE PROGRAM IN EARTH AND SPACE SCIENCE
YORK UNIVERSITY
TORONTO, ONTARIO

SEPTEMBER 2017

# Abstract

This research examines the feasibility of Commercial-off-the-shelf Complementary Metal-Oxide-Semiconductor image sensors for use on nanosatellites as a star imager. An emphasis is placed on method selection and implementation of the star imager algorithm: Centroiding, Identification and Attitude Determination. The star imager algorithm makes use of the Lost-in-Space condition to provide attitude knowledge for each image. Flat Field, Checker Board and Point Spread Function calibration methods were employed to characterize the star imager. Finally, feasibility testing of the star imager is accomplished through simulations and night sky images.

# Acknowledgments

I would like to thank everyone at York University who has helped me, from my days as an undergrad all the way through to my Masters. I would not have been able to complete this research without you. Specifically, I would like to thank Dr. Regina Lee (my supervisor) for all the support and for believing in me from the beginning. The guidance and help I have received from every faculty member at York has been extremely helpful in the completion of my research.

To all my friends and family at the university and beyond, thanks for all the fun times we have had, the distractions you have provided are a welcoming change from the constant focus of research. This venture has been a great experience and your support has made it easier to keep going. To everyone in the research group, past and present, your unweaving support has been invaluable in the completion of my research. I am grateful to have gained the friendships during this work that I know will last beyond. Finally, to my family thank you for the undying support and always helping me to push higher.

Lastly, a special thanks to Zoe for helping guide me through the task of writing this thesis.

# Table of Contents

# List of Tables

# List of Figures

# List of Acronyms

| | |
|---|---|
| AEC | Automatic Exposure Control |
| AGC | Automatic Gain Control |
| BCT | Blue Canyon Technologies |
| BSC | Bright Star Catalogue |
| CMOS | Complementary Metal-Oxide-Semiconductor |
| CPU | Central Processing Unit |
| COM | Centre of Mass |
| COTS | Commercial Off the Shelf |
| DCM | Direction Cosine Matrix |
| DSNU | Dark Signal Non-Uniformity |
| ESOQ | First Estimator of the Optimal Quaternion |
| ESOQ2 | Second Estimator of the Optimal Quaternion |
| FOV | Field Of View |
| FPGA | Field Programmable Gate Array |
| FPN | Fixed Pattern Noise |
| GTO | Geostationary Equatorial Orbit |
| ISS | International Space Station |
| LEO | Low Earth Orbit |
| LIS | Lost In Space |
| MST | Miniature Star Tracker |
| PCB | Printed Circuit Board |

| | |
|---|---|
| PPOD | Poly Picosatellite Orbital Deployer |
| PRNU | Photo Response Non-Uniformity |
| PSF | Point Spread Function |
| QUEST | Quaternion Estimator |
| ROI | Region Of Interest |
| SVD | Singular Value Decomposition |
| TS NST | Thin Slice Nano Star Tracker |

# Chapter One: Introduction

## 1.1 Problem Statement

Space has been a constant source of wonder and mystery to humans, driving scientific innovations to discover the "unknown". This drive to discover in the space industry has boosted the development of advanced satellite technologies in recent years. Much of this is due to the miniaturization of satellites, such as the class of CubeSat. CubeSats' light weight and simple design have allowed various industries access to a market originally unfeasible due to the financial costs required to launch a satellite. These satellites were originally developed as a low-cost platform to enable universities to access the space industry, providing researchers with hands-on educational opportunities to develop hardware and software for space applications. Though they allow many educational opportunities, CubeSat were largely incapable of achieving most space scientific objectives due to limitations in performance and were mostly used as testing platforms. Recent changes in financial global markets have shifted the role of small satellites to the front of the commercial world due to their combination of scientific potential but relatively much lower costs. The cost of launching large satellites is orders of magnitude greater than CubeSats. Companies and universities are now engaging together in research and business to increase the capabilities of CubeSats by implementing new technology and miniaturizing existing technology for use on CubeSats. However, in order to achieve current space scientific objectives or provide a useful service, CubeSat performance quality must approach the abilities of the larger-class satellites. Achieving large-satellite performance is challenging on CubeSats due to their much smaller volume and mass limitations. One aspect required to achieve high performance overall is high precision pointing accuracy from the attitude sensors. Performance

of the other onboard scientific instruments is irrelevant if the satellite has poor orientation information.

CubeSat design has favoured sun sensors and magnetometers attitude sensors for orientation determination over star cameras because star cameras tend to have more complex designs. Large amounts of resources are required for a star camera due to their complexity, often using large computational power and large physical volume for dedicated hardware. Star camera consumption of resources typically drastically limits the space allowed for other instrumentation, potentially reducing overall satellite functionality or the number of objectives that can be addressed. However, while advancing star camera technology has decreased size and power requirements over the past few years, many of these systems that are commercially available are still very expensive. In order for industry and universities to gain the most scientific benefits from CubeSats (and for government and private institutions to complete projects quickly and in a cost-effective manner), a Commercial-Off-The-Shelf (COTS) star camera with high precision attitude determination and low monetary cost is essential. The research in this thesis aims to develop and demonstrate the functionality of a COTS parts Complementary Metal-Oxide-Semiconductor (CMOS) camera by testing the pointing knowledge on real and simulated star images. Focus is placed on a system designed with commercial component rather than application specific components with high engineering cost. Leading to the development and implementation of a low computational system (eg., simple algorithm that requires less complexity).

## 1.2 Research Objective / Thesis Statement

The primary research objective of this thesis is to evaluate the ability of a COTS CMOS star imager for attitude determination on a Nanosatellite. Nanosatellites are a class of satellite

that have a wet mass ranging from one to ten kilograms. Within this class of satellite the standard form factor has become the CubeSat. The thesis focuses on selecting the individual methods required to construct the star imaging algorithm designed for a sensor to be implemented within a CubeSat. The general stages of a star imaging algorithm are centroiding, star identification, and attitude determination. The research objectives are to (1) identify the methods required to develop the star imager algorithm, (2) characterize the performance of the algorithm and (3) characterize the overall performance of the COTS CMOS camera. These research objectives are achieved through: development of the star imager algorithm through identifying in literature and implementing algorithm methods that are appropriate for CubeSat performance requirements; calibration of the hardware to determine the lens and sensor parameters; and characterization of the star-camera algorithm though a series of in lab and field tests.

## 1.3 Methodology

### 1.3.1 Thesis Framework

A CMOS star camera was developed (Irvin, 2014) with the use of an Field Programmable Gate Array (FPGA) for data acquisition in order to study the feasibility of star tracking with COTS parts (Irvin, 2014). In order to develop the algorithm architecture for the star camera, some preliminary work was required, including the selection of a lens with an increased focal ratio to enlarge the acceptance of light supplied to the sensor as determined from field studies of the original design (Irvin, 2014).

The star camera algorithm construction began with the review and implementation of existing methods developed for centroiding, identification and attitude determination. Determination of the selected methods started with a literature review of the methods used for star trackers and limited to methods that could be implemented on a nanosatellite. The next step

was to characterize the camera hardware through calibration techniques to help aid algorithm selection. Implementation of all algorithms was conducted using MATLAB as the language is a user-friendly mathematical environment that allows for fast implementation and demonstration. Using the MATLAB language also allows for a relatively simple integration into C, should the system eventually reach the next stage of development for a flight mode prototype.

Validation of the algorithms were conducted through a series of tests to characterize the limitations of the system. These tests allowed for refinement of the implemented algorithms to achieve optimal performance with the star camera hardware. To testing the algorithm functionality the use of simulated and real star images (static frame images) was implemented. Finally, the star camera was demonstrated during a field campaign in order to determine the functionality of hardware components and gauge the ability of the software to obtain attitude knowledge.

### 1.3.2 Hardware & Imaging Procedure

The hardware used for this research was the 24B752XA wide video graphics array CMOS camera designed on a 29 by 29 mm printed circuit board. This system is based on the 1/3" Micron MT9V022 sensor that has an active region of 752 by 480 pixels with a square pixel pitch of 6 micrometers. An Edmund Optics 58000 lens with 8.5mm focal and focal ratio 1.3 was used to provide an angular FOV of 31.8 degrees diagonal at infinite conjugate. A custom PCB was designed to transfer the low-voltage differential signal from the camera to the DE2-115 development board created by Altera which houses the Cyclone IV FPGA. The raw image data was transferred from the camera to the FPGA and a then finally a computer to retrieve and store images.

The sensors' internal registers were programmed using a PyCharm program. The camera continuously streamed data to the FPGA board which, when prompted, collects the next whole image when generated. The retrieval of the image was initiated on the computer with a MATLAB function and the data file was stored on the buffer of the FPGA board and uploaded to the computer once the entire image was registered. The collected images could then be processed immediately or saved to the computer.

### 1.3.3 Review of Initial Hardware Development

The work accomplished in (Irvin, 2014) provided a C-code to determine the sensor characteristics needed for star imaging in low illuminated conditions as well as an FPGA code that could read the image data from the CMOS sensor. A Monte Carlo simulation was also conducted to determine the FOV that the camera would require to observe three stars within any frame based on the star magnitudes, the tern 'sky coverage' was used to identify this observable area as shown in Figure 1 Sky Coverage versus Diagonal FOV (Irvin, 2014). The plot of sky coverage vs. FOV demonstrates that a camera with a FOV of approximately 31 degrees (used during this thesis) should be able to, in theory, observe enough stars in a single frame 22 % of the time with a magnitude three-star catalogue to obtain a successful attitude retrieval. Increasing the detectable magnitude limit of the camera system to a fourth or fifth star magnitude would increase the probability of detecting enough stars in a single frame to 80 or 100%, thus allowing the star imager to almost always have enough information to determine the attitude of the satellite.

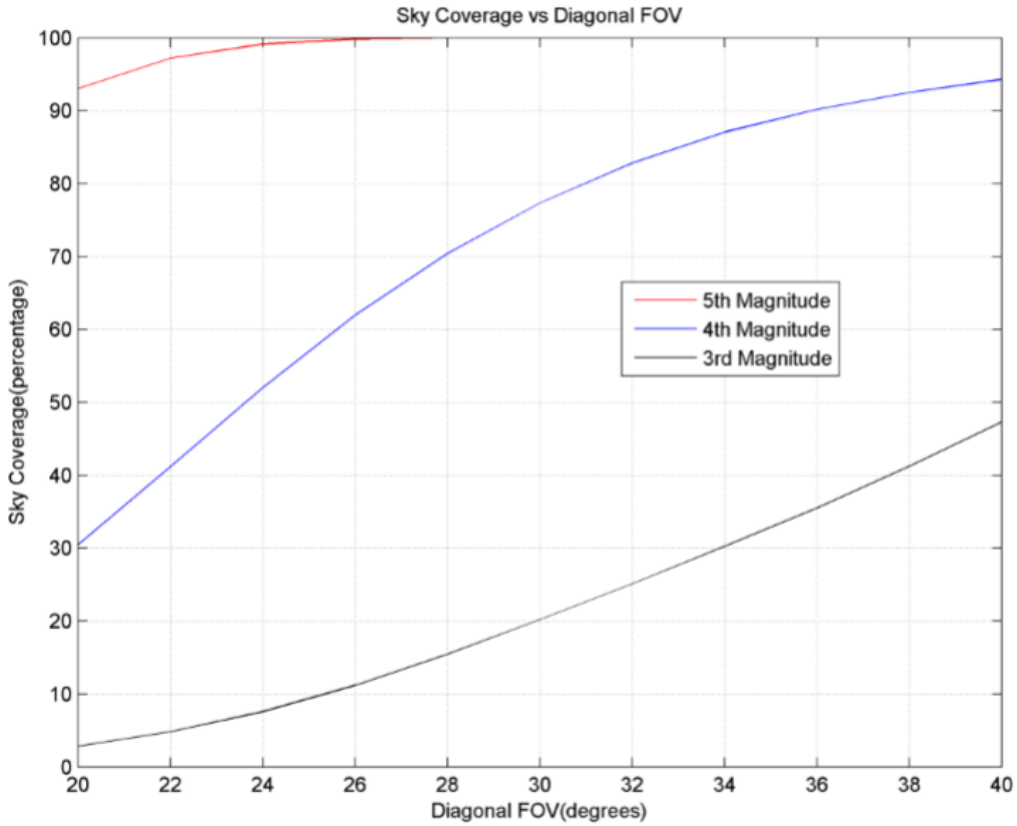


**Figure 1 Sky Coverage versus Diagonal FOV (Irvin, 2014)**

Nanosatellites with their small form factor have had limited exposure to the star tracker as an attitude sensors due to the large dedicated hardware required. In order to address the limited exposure star trackers are being designed to implement many different features from their standard heritage designs to decrease the power requirements and increase operation efficiency. This includes adding CMOS sensors and FPGAs into their hardware. The changes to a CMOS sensor reduce production costs and have improved readout abilities due to their individual pixel readouts. However, as a tradeoff due to its limited use compared to Charge-Coupled Device (CCD) sensors, the image quality and noise reduction capabilities of CMOS sensors have not been developed to the same standards (Sakakibara et al., 2005). Inclusion of an FPGA can increase the efficiency of the star imagers' capabilities by allowing for on-board re-configurable

designs or performing as a buffer for image holding and implementing basic computational processes on the image.

## 1.4 Thesis Outline

The research accomplished during this thesis is presented in seven chapters.

**Chapter One** covers an introduction into the research topic and its importance, the methodology applied to this research as well as a review of the previous characterization of hardware components from (Irvin, 2014).

**Chapter Two** provides a background on nanosatellites and their attitude determination systems. This section covers the sensors being used on nanosatellites with the focus on the star tracker and the current limits of star trackers implemented on these satellites.

**Chapter Three** reviews the noise and aberrations that are caused by optical systems and how they affect the performance of the system.

**Chapter Four** covers the selection of the centroiding, identification and attitude determination methods for the star camera algorithm. A summary of possible methods that could be implemented on a nanosatellite star tracker are compared and the selection of each method is detailed.

**Chapter Five** contains the calibration procedures and results for flat field, dark current, checker board, and point spread function tests.

**Chapter Six** covers the simulation and characterization of the star camera algorithm and the detailing of the field work campaign.

**Chapter Seven** contains the thesis summary and discusses application to the field of Nanosatellites as well as the possible future work.

# Chapter Two: CubeSat Standards

California Polytechnic State University developed the standard in nanosatellite deployment systems with the first deployment in 2003 attached to a Rockot (Pignatelli, 2014), the Poly Picosatellite Orbital Deployer (PPOD) as seen in Figure 2 Poly Picosatellite Orbital Deployer (Pignatelli, 2014). The PPOD was designed to allow for CubeSats to be arranged in multiple configurations, either a single 3U / 3+U or any equivalent combination. The PPOD system removes concerns about interfacing the Cubesat to the launch vehicle as it shifts the requirements from the nanosatellite developer to the developer of the PPOD system. The PPOD attaches to the side of the launch vehicle to allow for easy deployment upon arrival to the orbital location. There are many different deployment locations for nanosatellites. The conventional method is piggybacking on rocket launches to be deployed in Low Earth Orbit (LEO). More recently companies have utilised the International Space Station (NanoRacks, 2013) for deployment of nanosatellites as well as future plans to ferry these satellites to geostationary equatorial orbit (GEO) (Anon, 2017).

**Table 1 CubeSat Form Standards**

| | Length(mm) | Width(mm) | Height(mm) | Mass(kg) |
|---|---|---|---|---|
| 1U | 100.0 | 100.0 | 113.5 | 1.3 |
| 1.5U | 100.0 | 100.0 | 170.2 | 2.0 |
| 2U | 100.0 | 100.0 | 227.0 | 2.7 |
| 3U | 100.0 | 100.0 | 340.5 | 4.0 |
| 3+U | 100.0 | 100.0 | 340.5+ | 4.0 |

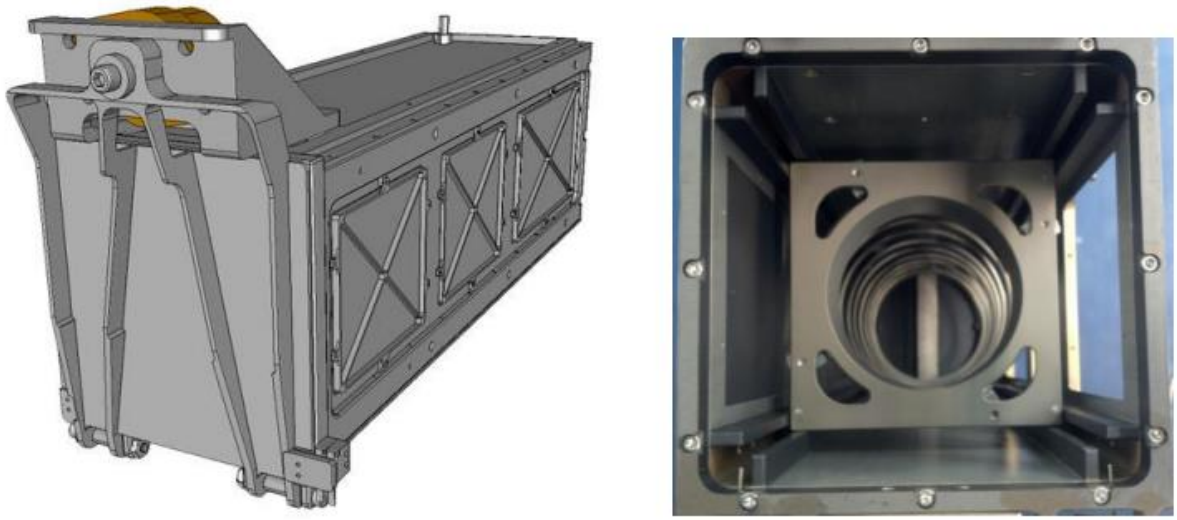

**Figure 2 Poly Picosatellite Orbital Deployer (Pignatelli, 2014)**

As the small satellite market continues to expand the forecast for expected launches of small to medium size satellites (1 – 50 kg) will reach a total between 1500 to 2500 during the period of 2016 to 2020. These predictions from Space Works indicate that the average growth rate in small satellite launches will be around 24% per year during this time (Doncaster and Shulman, 2016). As the market for small advanced satellites continues to grow star trackers will become instrumental components to ensure the success of attitude knowledge.

## 2.1 Attitude Determination

A spacecraft's attitude can be determined using different sensors (the different types of sensors are described later in this chapter). Many satellites employ more than one of these methods of attitude determination to ensure that maximum precision is achieved with robustness. Attitude Determination is the technique by which spacecraft in space determine their yaw, pitch and roll, characteristics that describe orientation. A spacecraft's orientation is a critical parameter that must be correctly determined as many sub-systems depend on this information. Some of these systems include solar panels that collect energy by facing towards the sun and antennas for

communications that need to point towards other satellites or ground stations to transmit data. There are many other payload systems that depend on accurate pointing for scientific data acquisition and function at optimal performance when their orientation is correctly aligned.

The task of attitude determination can be separated into two categories (Serway et al., 2000). The first is the "lost in space" (LIS) case where the satellite has no a-priori information on the attitude. The complexity of this case is often computationally taxing on the Central Processing Unit (CPU) requiring a large amount of data to be processed. The second case is when the current orientation of the spacecraft is predicted by using the reference of a previously known attitude measurement. The prediction of the attitude knowledge is possible as the attitude of the spacecraft was initially determined in the LIS case and is switched to a tracking method. The tracking method requires less computational power as the LIS method has narrowed the search region by providing prior information. The two methods described above both use the knowledge of the satellites (body) frame combined with that of the inertial frame will give rise to a unique attitude solution. There are many different sensors that are capable of determining ones' attitude but star sensors are preferred for their high degree of accuracy.

## 2.2 Attitude Sensors

There are many different sensors that are used for attitude determination some of these include sun sensors, horizon sensors, star sensors, rate gyros and magnetometers. While many of these systems provide the information required to calculate the attitude of the system, they all suffer from some drawbacks. A large problem that sensors like the gyro experiences is the systematic drift from small errors that compound on its measurements over time. Sensors that use an optical design such as the star sensor do not have this issue as they calculate their position during every frame and only use appended

material to estimate the last known measurement. This section will cover a brief review of the most common sensors implemented in CubeSat's.

### 2.2.1 Sun Sensor

The most common sensor for attitude determination in space missions is the sun sensor (Bouwmeester and Guo, 2010). The sun sensor is a device that can provide two axis attitude knowledge of a satellite by using the sun as a reference through the incident ray angles. Multiple sun sensors are often mounted on the satellites outer panels reducing the number of solar cells, thus having a large impact on the power generated on smaller satellites. There are three main types of sun sensors: the analog sensors, digital sensors, and the sun presence sensors. While digital sensors are the most accurate type of sun sensor they are also the most expensive. Analog sensors are the most common as they provide moderate quality detection for their relatively lower monetary cost.

### 2.2.2 Magnetometer

Magnetometers are one of the most common sensors on nanosatellites (Bouwmeester and Guo, 2010). These sensors measure the intensity and direction of the Earth's magnetic field. They are light weight, small sensors that do not require much power for operations. The Earth's magnetic field extends for several thousand kilometers above the planet's surface but due to its sudden decrease in intensity at higher altitudes this makes magnetometers often unusable beyond LEO.

### 2.2.3 Gyro Rate Sensor

The rate sensor is unique compared to the other sensors listed above as these sensors measure the angular velocity and do not provide a satellite with direct attitude information. Gyros do not require any external source or reference point and are placed in the interior of the

satellite where a sensor is used for each axis. Prior knowledge of the satellites pointing direction must be known for continuous attitude information. A disadvantage of these sensors is that the continued use over time leads to a compounding drift factor with no external reference point the compounding drift cannot be mitigated. For this reason, rate sensors are always paired with another sensor such as a magnetometer that can provide a reference point to an external measurement to determine the satellite's attitude.

### 2.2.4 Horizon Sensor

The horizon sensor is an infrared camera that determines the contrast boundary between the cold darkness of space and the heat produced from the Earth. The sensor then orientates the satellite relative to the Earth's horizon.

### 2.2.5 Star Camera

The star camera or tracker is a camera based attitude determination system that can use either a CMOS or a CCD sensor, the latter being more common. The sensor is used to take images of part of the sky that are then compared with a catalogue of a known star map. These systems have several drawbacks, including: their complexity of design, high cost, intensive computational algorithm and their sensitivity to bright sky objects. Sources such as the moon, planets and sun can saturate the sensors and interfere with orientation calculations. The star camera is the most accurate of the attitude determination sensors with the ability to determine arc-second accuracy when there isn't interference from bright objects.

### 2.2.6 Sensor Accuracy Comparison

Here is a summary of the sensors above and their associated accuracies.

**Table 2 Attitude Sensor Accuracies (Wertz and Larson, 1999)**

| Sensors | Accuracy |
|---|---|
| Sun Sensor | 0.01° |
| Star Sensor | 0.0028° |
| Horizon Sensor | 0.1 – 0.05° |
| Magnetometer | 1 – 5° |

## 2.3 Star trackers -Historical Development

Star trackers have changed drastically since their development from single slit star trackers to V-slit and then the modern trackers of today that image a star field. The first star tracker was designed to provide attitude knowledge in two axes (Birnbaum et al., 1980). This first star tracker required the cooperation with other attitude sensors to provide the other degree of freedom needed for attitude determination. The star tracker worked by selecting a bright star that fell within the FOV of the sensor as the star tracker was oriented 90° to the adjoining attitude sensor.

An evolution of the star tracker came when the V-slit was designed. This design was unique as it required the satellite to spin to provide attitude information. The V-slit works by having a star cross over the two slits of the sensor. As the star moves across the sensor, the location and brightness of the star are used to determine the attitude knowledge (Wertz, 2012).

Today's modern star trackers have the advantage of modern sensors that allow for large areas of the sky to be imaged, thus allowing for trackers to locate several stars in a single frame.

These stars can be grouped to produce unique clusters of stars that are then referenced to a database which provides the satellite with accurate attitude knowledge. These star trackers removed the need for a spinning satellite and the addition of complementary components to achieve the attitude solution allowing for a simpler satellite.

The newest star cameras improve capability under conditions that star cameras would normally have poor performance. In atmosphere star cameras under daylight conditions are unable to identify individual stars because of pixel saturation. Research into star cameras to perform day light tracking through the atmosphere is underway (Hille, 2015). The motion of satellites reduces the accuracy of star imaging for high magnitude stars by causing image smearing, which results in a poor PSF. Ball Aerospace has designed the High Accuracy Star Tracker that can maintain its lock on a star despite motion of the satellite up to four degrees (Aretskin-Hariton and Swank, 2015). These star trackers are some of the most advanced designed in the field but are beyond the scope of this thesis.

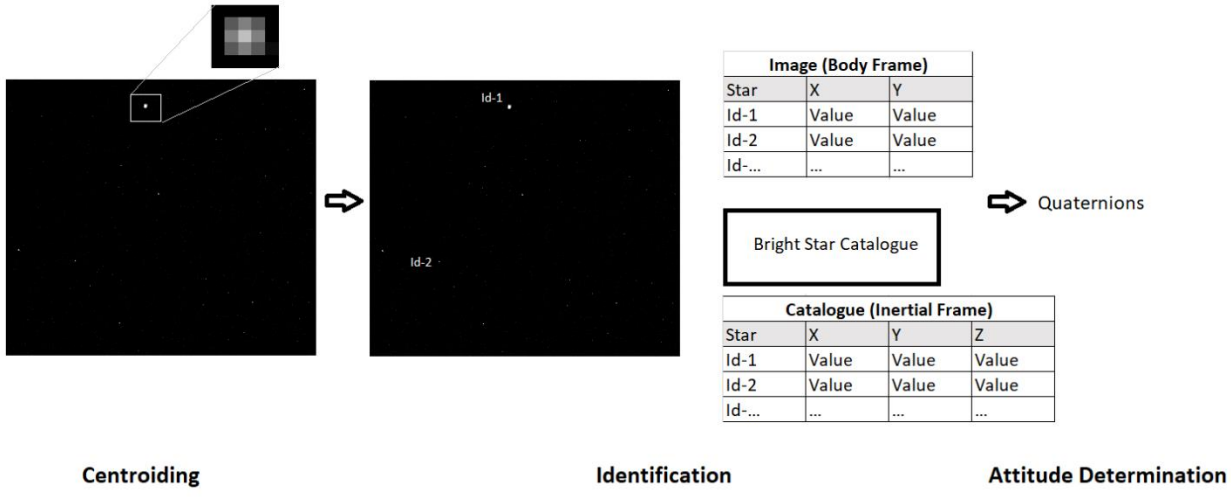


**Figure 3 Schematic of the Modern Star Tracker Algorithm**

### 2.3.1 High Accuracy Star Trackers

All subsystems of a satellite must deal with constraints that limit the resources available these include mass, power consumption and volume. Some specific constraints for star images are their pointing accuracy and update rate. The complexity and resources required have long limited the use of star imagers in nanosatellites with new advanced designs and creative algorithm construction. This is no longer the case. Below is a list of some of the most efficient and best performing star imagers.

**Table 3 High Performance Star Trackers for Small Satellites**

| **Manufacture** | Hyperion Technologies | Hyperion Technologies | Blue Canyon Technologies | Sinclair Interplanetary | Azmerit ltd. |
|---|---|---|---|---|---|
| **Model** | ST-200 | ST-400 | Thin Slice Nano Star Tracker | ST-16RT | AZDK-1 |
| **Mass** | 0.05 kg | 0.21 kg | 0.20 kg (with baffle) | 0.16 kg | 0.12 kg * |
| **Power** | Avg <700mW Peak 1W | Avg <700mW Peak 1W | Avg <1.2 W Peak <1.5W | Avg < 0.5 W Peak 1.0 W | Avg 0.25 W ** |
| **Volume** | 30 x 30 x 38 mm (excluding baffle) | 53.8 x 53.8 x 90.5 mm (excluding baffle) | 100 x 100 x 30 mm (with baffle) | 62 x 56 x 38 mm | 40 x 40 x 71 mm |
| **Update Rate** | 5 Hz | 5 Hz | 5 Hz | 2 Hz | 10 Hz |
| **Accuracy (Bor. & Roll)** | 30” & 200” (3 sigma) | 15” & 120” (3 sigma) | 6” & 40” (1 sigma) | < 4” & <30” | 10” & 70” |
| **Baffle** | Mission dependent | Mission dependent | Integrated Baffle | Mass: Small 0.030 kg Large 0.071 kg | N/A |

*(without cable, its connector and a cover) ** (when the thermo-electrical cooler is off)

Blue Canyon Technologies (BCT), Hyperion Technologies and Sinclair Interplanetary star trackers can be purchased as complete packages that are virtually (black box) plug and play ready (Erlank, 2013). The AZDK-1 created by Azmerit ltd. is designed using Russian electronic

components and is the only system from the high-performance group that requires cooling for its operations (Kerimovich, n.d.). Comparing the features that were listed above, the first three star imagers from the left are very similar in capabilities and resources required.

Hyperion Technologies, creator of the ST-200 and ST-400, were designed in cooperation with Berlin Space Technologies GmbH. The ST-400 is an improved version of the ST-200 that is specifically designed for Pico and Nano satellites. The 400 series were designed for microsatellites or larger, however due to its relatively small forum (50x50x100mm) it can still be used for nanosatellites. Both systems feature an internal gyro system that allows for the determination of the slew rate up to 200 degrees per second even without a visual lock on a star (Erlank, 2013).

The Thin Slice Nano Star Tracker (TS NST) was developed by BCT and is also an upgraded model from their standard Nano Star Tracker (NST). The TS NST has most of the features as the older NST other than the new design which reduced mass. The TS NST is a board design which limits the orientation of assembly. BCT manages to get high performance in its design by including a catalogue of over 20,000 stars or magnitude 7 and a 9 x 12 FOV (Blue Canyon Technologies, n.d.).

The Sinclair Interplanetary ST-16RT co-created with Ryerson University's Space Avionics and Instrumentation Lab (SAIL) and Space Flight Laboratory of the University of Toronto Institute for Aerospace Studies. The ST-16RT uses a 5 megapixel CMOS sensor with a 20 x 15 FOV which allows for the imager to have such high performance (Dzamba, 2013). The ST-16RT has a newer lens system which is expected to increase performance and is beginning shipping orders to customers in Q3 2015. Sinclair has used a couple of different methods to achieve its performance ability. First it uses a lost-in-space search mode for each frame

calculation and never transitions to a tracking mode. Secondly it reboots after every frame to mitigate radiation induced memory upsets and lastly the image sensor uses a rolling shutter instead of a snapshot shutter (Dzamba, 2013).

AZDK-1 manufactured by Azmerit ltd created their prototype in Q2 of 2015. Azmerit has designed its imager with a thermoelectric cooler, which without any known space flights it statistics cannot be assumed 100 percent accurate (Kerimovich, n.d.). AZDK-1 has a 20 degree FOV with a star catalogue of 2,200 stars or magnitude 5.5

### 2.3.2 Lower end & Concept Star Trackers

The star trackers listed above are all corporate built systems which have a high associated cost with them. While, the list below covers star tracker designs that incorporated university collaboration into the design or construction phase.

**Table 4 University Constructed Star Trackers for Small Satellites**

| **Manufacture** | AeroAstro | University of Wuerzburg | Stellenbosch University |
|---|---|---|---|
| **Model** | Miniature Star Tracker | STELLA | CubeStar |
| **Mass** | 0.38 kg | 0.12 kg | 0.09 kg |
| **Power** | Avg < 2W | 0.2 W | Avg .35W<br>Peak .55W |
| **Volume** | 60 x 76 x 76 mm | 60 x 46 x 58 mm | 46 x 33 x 70 mm |
| **Update Rate** | 2 Hz | 4 Hz | 1 Hz |
| **Accuracy (Bor. & Roll)** | 70” | 0.6’ & 2.4’ | 0.6’ & 1.8’<br>(1 Sigma) |
| **Note** | | | Without enclosure or baffle |

The Miniature Star Tracker (MST) developed by Comtech AeroAstro and Massachusetts Institute of Technology and was designed around 2003 (Carroll et al., 2004). The MST was constructed to fill the gap between large satellite star trackers and very coarse sensors. Since this was an early design, the imager only uses a 1 megapixel CMOS sensor which can only detect

magnitude 4 stars. The MST achieves its performance by using a 30 degree FOV (Carroll et al., 2004).

STELLA (Fischer et al., 2014) created by the University of Wuerzburg in Germany passed qualification testing in 2012. STELLA uses a similar design concept to the ST-16RT that allows the system to reload entire software for all embedded processes, removing any damaging effects caused by radiation.

Stellenbosch University in South Africa is the developer of the CubeStar star tracker (Erlank, 2013). This is a first-generation star tracker and a modified second generation is expected to be completed in 2015 to fly on ZA-AeroSat for QB50. CubeStar is capable of detecting stars down to magnitude 3.8 with a 51 x 27 degree FOV.

## 2.4 Star Tracker Functioning Factors -Limitations

There are several factors that limit the operational properties of any component in space. This is true with the star camera as well, with each section of the star camera having its own specific instrument limitations. Internal factors that affect the performance of the camera system include design decision, noise sources and lens aberrations. The noise and lens aberrations will be covered in the next section in this thesis. However, there are also several external factors that impact the star camera's performance. These factors need to be considered when designing the system because some of them can be mitigated through design choices. A summary of some of these factors are listed in this section but will not be covered in detail as these factors were not the major focus of this thesis.

The following are some examples of external factors and associated design decisions that attempt to mitigate their impact.

- The detectable magnitude of the sensor is an important limiting factor that affects the number of stars visible within the FOV. If a sensor has a limiting magnitude of four, then the approximate number of visible stars in the celestial sphere is five hundred. This design decision forces the FOV of the camera to increase in size to ensure that the star camera can maintain a set of three stars within the FOV during operation. Otherwise, it risks reducing the rate at which an attitude measurement can be collected.
- The spectral distribution of the PSF of the instrument. The PSF describes the distribution of a single point of light on the sensor (Discussed in Chapter 6 Calibration). The PSF is used in the centroiding algorithm to ensure the best estimates are calculated.
- The equal distribution of the stars relative to the pointing direction of the camera. Stars should neither be too close to the center of the image plane or to close to its edges. In order to have consistency in star measurements the stars should fall within a ring around the center. This is a constrain that is decided before the star selection for the matching algorithm.

  External limitations are factors that may not be mitigated but should not be over looked during designing a star tracker, these include:

- The star tracker algorithm will have to account for any disturbances created from all non-stellar objects, such as satellites or space debris in higher elevations passing through the FOV.

- The reference catalogues of the matching algorithm have a positional accuracy of stars that can vary between 10- to 40-milliarcseconds (Lee et al., 2005). The variations in positional accuracy are a limiting factor in attitude determination as the reference source to which a measurement is made contains an error.
- The image smear and angular rate of the stars relative to the pixels' orientation causes the star light to spread across several pixels causing a streak to appear on the image plane. This spread of pixels can cause the centroiding algorithm to incorrectly estimate the centre of a star.
- The optical surface is cleaned before deployment to mitigate stray rays of light from becoming focused onto the image plane. Dust and other debris on the lens can cause a star camera to image dust rings that affect the measurement of stars.

# Chapter Three: Noise and Aberrations Background

This section will cover the background information on some of the different types of noises and aberrations that affect the performance of the star camera system. Noise sources are caused by fluctuations in the electronics that obscure the incoming transmitted signal resulting in an electrical transmission that deviates from the expected signal. These noise sources can be separated into two main categories: temporal and spatial noise. The noise generated from these two classifications affect the image output of our image differently but they both cause the "true" signal created by the photon flux incident on a sensor to vary from the true signal. As these added components alter the true signal, the resulting measured signal might contain distortion in the stars' positions, resulting in a deviation in the reported star location from the true location. Aberrations are caused by the optical system and are due to the actual performance of the hardware compared to its ideal performance. Aberrations that affect the performance of the system are described towards the end of this chapter.

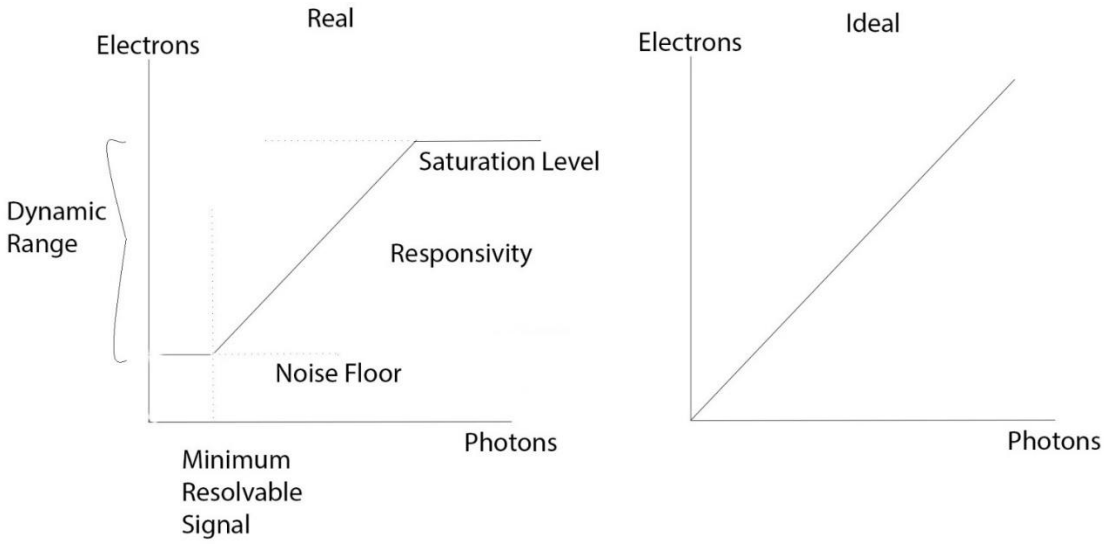


**Figure 4 Real versus Ideal Sensor Performance [Adapted from (Hornsey, 2008)]**

The ideal case for photons converted to electrons is represented in Figure 4  Real versus Ideal Sensor Performance [Adapted from (Hornsey, 2008)] where an image has a one-to-one conversion rate. However, in reality noise plays a large role in determining the quality of an image. Noise impacts detection limits, which determines the minimal resolvable signal. Any photons collected below this limit cannot be deciphered from the background noise that is always present. The top end of the detectable limit is the saturation level where the sensor has reached its maximum responsivity to incoming photons. The top and bottom regions of the detectable limit create a boundary known as the 'dynamic range', which is where the sensor will operate.

## 3.1 Temporal Noise versus Spatial Noise

Temporal noise summarizes all the noise sources that influence the values of a pixel from frame to frame regardless of what is imaged.  Temporal noise is normally the dominant source of Charge-Coupled Devices (CCDs) as the readout of a CCD has its charge shifted many times along the row of pixels until the charge reaches the readout circuitry. Temporal noise is created from dark shot noise, photon shot noise, reset noise, and amplifier noise. Spatial noise is characterized as time invariant noise. This type of noise is caused from Dark Signal Non-Uniformity (DSNU) and Photo Response Non-Uniformity (PRNU). CMOS sensors tend to be dominated by spatial noise as each pixel has its own readout circuit. Spatial noise sources can be measured and their effects mitigated through calibration techniques while many of the temporal noises are due to the architecture of the image sensor and therefore, cannot be mitigated as easily.

CMOS sensors have a higher noise component than CCD due to the additional components in its design as every pixel has one or more transistors. These extra transistors cause temporal noise to be the fundamental limiting factor on performance of the system under low illumination (Tian, 2000).

## 3.2 Spatial Noise

### 3.2.1 Dark Signal Non-Uniformity - Fixed Pattern Noise

DSNU is the variance in dark signal across the pixels. It remains fixed between frames and is independent of the pixels signal. CMOS sensors are greatly affected by DSNU because of the inconsistencies in pixel component quality and associated readout circuitry for each pixel. DSNU has two components that contribute to this noises creation: thermal and electrical. The thermal component is dependent on the temperature and integration time. The electrical component is dependent on the integration time and the various imperfections of electrical hardware. In order to measure and mitigate DSNU of a sensor, multiple frames in the absence of illumination are required. Averaging these frames reduces the thermal noise of the dark frame images. Using the averaged frame a function can be implemented to increase or decrease each pixels base values when compared to the mean value (Toczek et al., 2013).

### 3.2.2 Photo Response Non-Uniformity

PRNU is the variance across the pixels under illumination. This noise is due to the physical properties of the sensor where small variations in materials or size of each pixel cause the pixels to respond to incident photos differently. In the ideal case with a uniform light, all pixels should read an identical value but, due to PRNU the values vary across the pixels. In a similar method used to measure the value of DSNU, the PRNU is estimated using multiple images using a uniform light exposure. Averaging the images to reduce the thermal noise of the resulting images and the standard deviation of the pixel signals allows an estimation of the PRNU magnitude.

## 3.3 Temporal Noise

### 3.3.1 Photon Noise

Photon shot noise is generated from the random photon flux incident on the image sensor. The noise shows a Poisson distribution and has a square root relationship between the amount of signal and noise. This means that noise is directly dependent on the number of photons that fall on the image. Therefore, this noise can only be reduced by increasing the number of photons as the noise value is relatively weaker at higher signal levels. Photon noise is generally a contributor to overall error in an image under low light conditions (Hasinoff, 2014).

$$photon\ noise = \sqrt{number\ of\ photons}$$

### 3.3.2 Dark Current

Dark current originates from release of electrons generated from thermal energy in the sensor. Dark current is proportional to the increase in exposure time as well as temperature. Therefore, dark current noise can be reduced by cooling the sensor to mitigate the excess energy in the pixels. Dark current is modelled using a Poisson distribution as shown in below.

$$dark\ noise = \sqrt{(dark\ current)(integration\ time)}$$

### 3.3.3 Readout Noise

Readout noise is caused by the process of quantifying an electronic signal. Photons incident to a sensor are collected within pixels that are converted from an electrical charge to a voltage measurement. CMOS sensors perform the conversion on a per pixel bases as each pixel has an individual readout systems for converting the charge to a voltage. These individual readout circuits have an amplifier to increase the voltage signal before the analog to digital conversion occurs. The process of amplifying the signal (measuring the amplified signal) causes

small fluctuations in the measurement. The CMOS sensor therefore has a distribution of amplifier signals as the inherent property of each circuitry is slightly different from pixel to pixel.

### 3.3.4 Quantization

Quantization noise is due to the uncertainty in the electron value generated from the analog-to-digital conversion. The conversion from a continuous signal to a discrete signal forces values of the continuous signal to a finite structure. This creates an error in the system as the values are randomly binned higher or lower than their actual value.

### 3.3.5 Reset Noise

Reset noise is caused by an inaccurate voltage measurement following the readout after a pixels' integration. This error in the reset value is due to a thermal influence of the circuitry. The reset voltage prior to a new integration represents the minimal voltage floor of the pixel. The incorrect reference to the voltage floor causes a decrease in the ability for the sensor to detect during low-illuminated conditions. The reset noise can be expressed as:

$$n_{RMS} = \frac{\sqrt{kTC}}{q}$$

Where q is a single charge of one electron, k is Boltzmann's constant, T is the absolute temperature and C is the capacitance (Calizo, 2005).

## 3.4 Aberrations

### 3.4.1 Distortions

Distortion is an optical aberration that causes a lens or lens system to incorrectly project information. This deviation of information from the lens system causes an object to be projected to a different location on the image plane than is intended. The optics of a lens system

determines the extent of the distortion, as a greater distortion is often contributed to a larger FOV due to the increased field dependence. There are two types of distortions shown in Figure 5 Distortions from Lens (Mahajan, 1998) these distortions are classified by the positive (Barrel) or negative (Pincushion) movement of information from the centre of an image. This geometric distortion can be mapped and mitigated as none of the information is destroyed due to the incorrect projection. These distortions can cause a misidentification of the stars when compared to the star catalogue since the triads position is translated incorrectly.

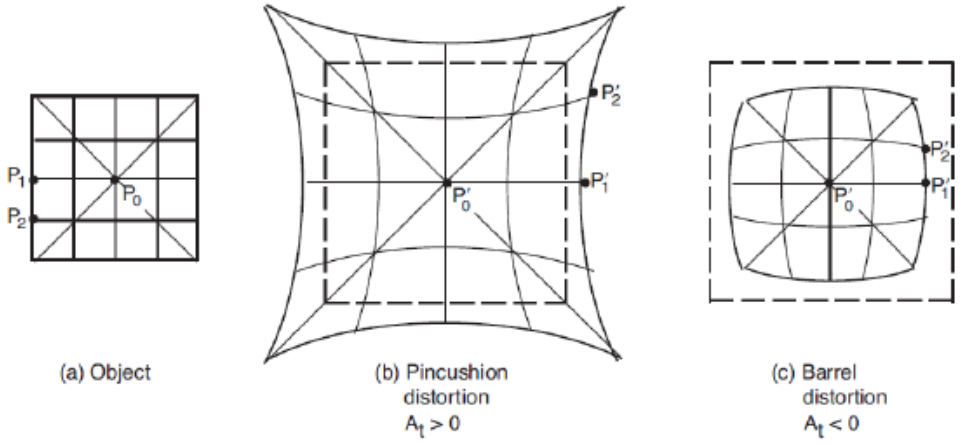


**Figure 5 Distortions from Lens (Mahajan, 1998)**

### 3.4.2 Astigmatism

Astigmatism occurs when the propagation of star light in two axis each have a different focal distance. This aberration caused the horizontal and vertical projections of the star in the image plane to appear in different locations along the focal plane. The resulting projection from astigmatism on an ideal star cause the circular light pattern to appear as an ellipse. This type of aberration increases with increasing distance from the centre of the lens (Malacara et al., 2004; Sasian, 2013).

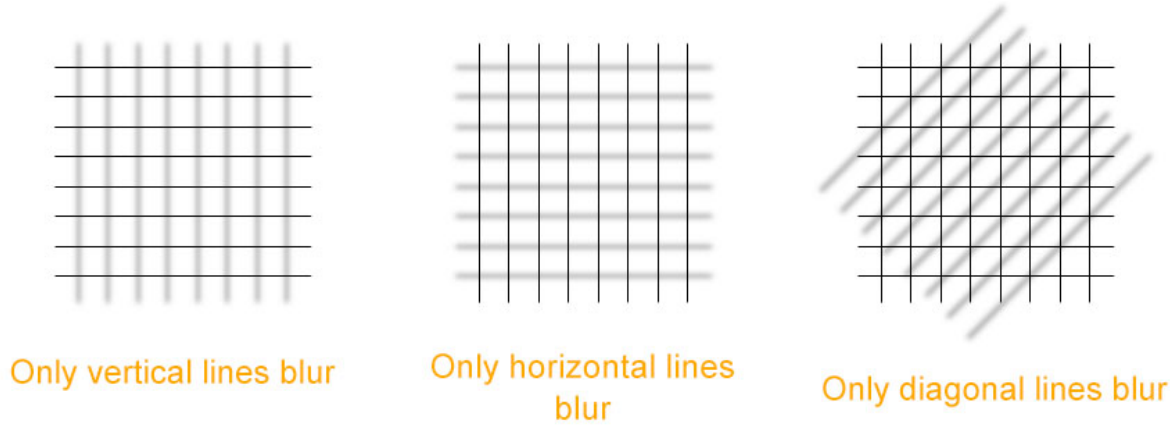


**Figure 6 Astigmatism Affects from Lens (Sudhakaran, 2013)**

### 3.4.3 Field Curvature

The field curvature is caused from the spherical shape of the lens as it projects the image on to a flat surface (the sensor). This spherical shape in the lens causes the light to focus in front of the image plane as the foci moves away from the centre of the frame. The resulting effect is that an elliptical deformation of the star image occurs, decreasing the probability of a successful centroid of the star as the edge of the star is blurred in relation to the centre.

### 3.4.4 Lens Coma

Comatic aberration is caused by imperfections in the lens construction, which vary the magnification of incoming rays to different foci, creating a tail like effect on the star in the image plane.

### 3.4.5 Spherical Aberration

Spherical aberrations are an optical effect that is due to the difference in refraction of light rays as they move through different locations on a lens. The outcome of this aberration is the focal point for different parts of the lens focus either in front or behind the image plane.

# Chapter Four: Star Camera Algorithm

## 4.1 Method Selection and Design Factors

The flow chart below illustrates the outline of this chapter and the different methods that were considered for each sub-algorithm of the star camera. The methods of each sub-algorithm are described and then inter-compared to determine the most suitable method for implementation.

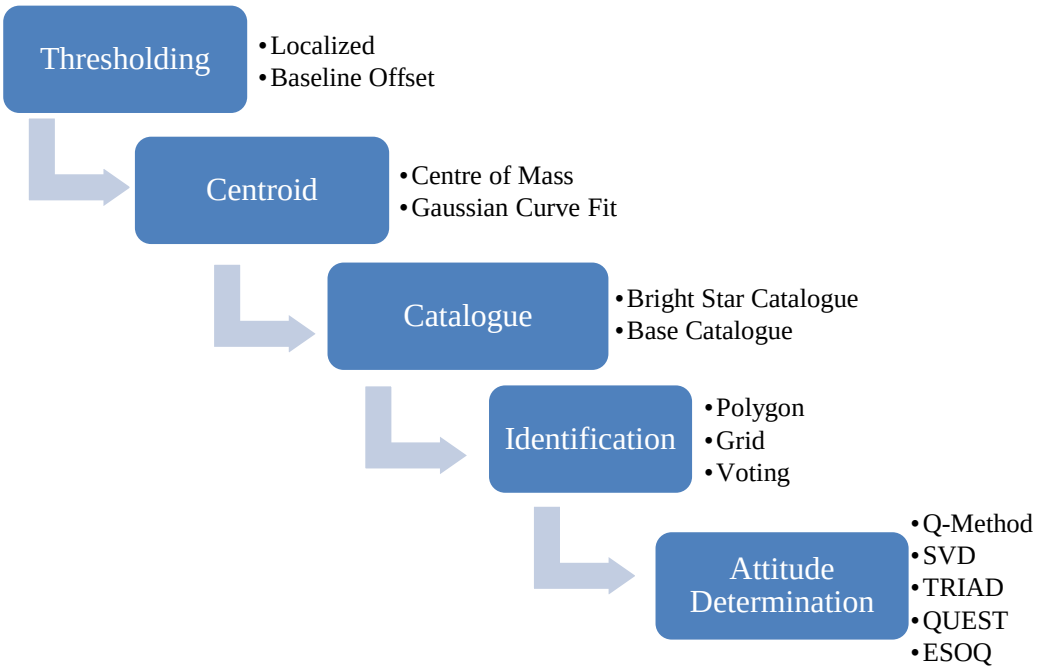


**Figure 7 Star Imager Algorithm Flow Chart with Methods**

The star camera algorithm consists of several sub-algorithms, which each have different design elements that must be taken into consideration to achieve overall optimal performance. Tailoring these design elements is dependent on the type of performance a star camera is required to achieve. This research uses COTS components which require the algorithms to be robust as potential fails may occur during the operational life of the components. However, the proposed star camera design is implemented in a nanosatellite it must also be efficient to reduce

power consumption. The implemented methods for the sub-algorithms will be covered within this chapter explaining the design choices.

When designing an algorithm, the associated characteristics of noise and computational error must be kept in mind while selecting the methods for implementation. These are potentially present at every stage of the algorithm construction and need to be mitigated as much as possible to ensure the best result is determined. With many potential sources of error stemming from the hardware of the system it is very important to have an algorithm that performs with a high degree of precision and accuracy.

The computational time of the algorithm is an important factor that must also be considered to ensure that all electronics are working in tandem. Slow computational times or "time delays", can limit optical pointing knowledge of the star camera as the temporal frequency of image capture can be significantly limited by the processing time. An example comes from the centroiding algorithm as this is an intensive process and requires a lot of bandwidth, which is limited for nanosatellites due to their small form factor. A dedicated processor is often an option to mitigate time delays but nanosatellites cannot necessarily accommodate the additional power, mass, and volume associated with adding another system. Therefore, the optimal choice is to determine an algorithm that can reduce computational time. There are many techniques for the centroiding algorithm, which vary in computational time as some algorithms have increased performance and robustness at the expense of processing time. It is important to determine the optimal balance between algorithm performance and computation time in order to achieve a system that meets the mission criteria.

## 4.2 Thresholding Method

The star camera algorithm starts with retrieving the raw image for centroiding. Before the image can be applied to determine the location of stars it was adjusted for imperfections in the hardware and electronic components by applying a calibration map to the raw image. Calibration procedures will be explained in a following chapter.

After adjusting the image for imperfections, the identification of star locations in the image plane is conducted. In order to accomplish this task, a threshold determination method is implemented to scan across the image file and determine which pixels pass a given criterion for the thresholding conditions. The basic assumption of this method is that a pixel that passes a brightness threshold will represent some part of a star. In order to determine the signal brightness value for the threshold, a standard deviation of the entire frame (intensity matrix) is used (Huffman, 2006). This value defines the brightness limit required for a pixel to be considered a star. With this implementation, the intensity values over a sigma value range of two or three is considered a star as they have a much higher brightness than the frame average brightness value. The sigma value used is determined through experimental testing and will vary due to the properties of the optics and sensor. As the optical system quality is increased the difference between background noise and star light become increasingly more distinguished, reducing the need to increase the thresholding factor above the background noise. However, since a hot pixel can pass the threshold for star determination, there must be another condition for pixels to be considered part of a star. The most common method and the one employed during this research is to check the pixels adjacent to the test passing pixel. A star should be represented by several (approximately four to nine pixels determined through Point Spread Function (PSF) parameters for this research – results of the PSF are discussed chapter 6 calibration) pixels that are clustered

together that also pass the testing conditions. The PSF is a property of the optical setup and can be determined before algorithm construction.

Once the signal threshold condition of a star has been defined, a recursive search is performed to find all (if any) stars in the image to pixel accuracy. In order to ensure that an accurate number of pixels clustered together are checked through the recursive search algorithm, the use of the PSF patterning is taken into consideration to determine the size of the pixel array. The recursive star search algorithm for this research checked a three by three array of pixels and compared the brightness values. If a brightness value of a single pixel was greater than the signal threshold, the 3 by 3 search array is centred on that pixel and compares its signal to the surrounding pixels' values. If a brighter pixel was found beside the current pixel of interest, the process is started again with the Region Of Interest (ROI) centred on that new location.

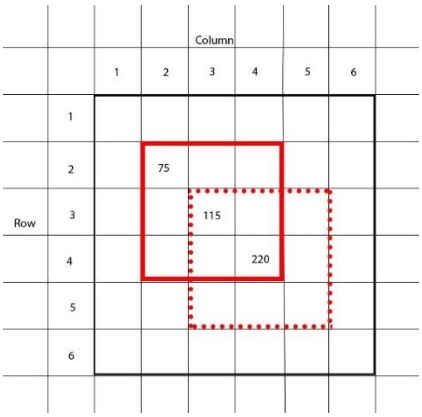


**Figure 8 Centroiding Algorithm, ROI Selection**

This process estimates a star's location by finding the brightest pixels in an image. The thresholding algorithm produces a checked list of locations that the search algorithm has visited to ensure search algorithm efficiency. The algorithms efficiency is increased by the fact that the ROI is a three by three grid. This allows for every other row and column to be searched as the adjoining row and columns will have been searched due to the grid size. Once the location of

potential stars has been detected, a centroiding algorithm is implemented to calculate the subpixel location.

Depending on the methods implemented in the matching algorithm the thresholding process can be modified to search specific quadrants of the image first or stop searching entirely after the required number of stars needed for the matching method has been achieved. This fine adjustment to the code can be advantageous in decreasing the processing time of the identification stage.

## 4.3 Centroiding Method

### 4.3.1 Centroiding Noise Mitigation

Performing this operation with focused light will lead to the incident photons being measured on one or two pixels, resulting in pixel saturation. This pixel saturation limits the performance of the centroiding algorithm to pixel level accuracy. With all of the light appearing on a single pixel there is no further information available to determine a more accurate centroid. In order to increase this accuracy to the sub pixel level, the stars' light is intentionally defocused to spread the brightness of a star over several pixels. The precision of sub-pixel accuracy is approximately 0.1 of a pixel or better (Kandiyil, 2009). Reducing errors in the centroiding algorithm is important for accurate attitude determination because this error propagates through the entire star camera algorithm. Since this error is a product of an earlier sub-routine, it has the potential to impact the final accuracy of the attitude determination more than an error created in a later sub-routine. This potential for a larger impact is due to the cascading effect an early error may have, however, there is also the potential for a very large error in a later sub-routines that overpowers any cascading error.

The background noise in every image is removed to ensure an accurate centroid. This can be accomplished in two ways: the first is a localized average subtraction around the selected centre pixel. This method removes the localized noise around the centroiding location by averaging the adjacent pixels to centre pixel to determine the background noise. This method provides an accurate mitigation to the systems noise effects of the sensor by working in a smaller region. However, added computation time is required as many smaller tasks are performed to mitigate noise with many stars in a frame. The second approach assumes a baseline 'offset' of the brightness of the entire image. The image is assumed to have an even distribution of noise across all pixels and saves computation energy by only creating a single background for the whole image. Computation time can be further reduced by assuming that the background noise remains constant for multiple images. The baseline offset approach was implemented as the centroiding noise mitigation method for this research because image testing of the background noise value indicated that background noise was constant for multiple frames. The other factor that affected decision was the limited processing capabilities of most CubeSats.

### 4.3.2 Centroiding Methods

Centroiding algorithms commonly use one of two general methods to estimate the location of the centre of the star beyond the pixel level: Centre of Mass (COM) method and a Gaussian curve fitting method (Delabie et al., 2014). The Gaussian curve fitting method fits a Gaussian function to the shape of the dispersed light on the sensor over the pixel region identified as containing a star. Once a Gaussian curve is fit, the star centroid is assumed to be at the location of the peak of the gauss function. A catalogue of all Gaussian peak values is usually stored onboard the satellite. This method is more accurate than the COM method as the incident

light on a sensor is ideally of a Gaussian distribution, however this method requires greater computational power to fit a Gaussian curve to the input.

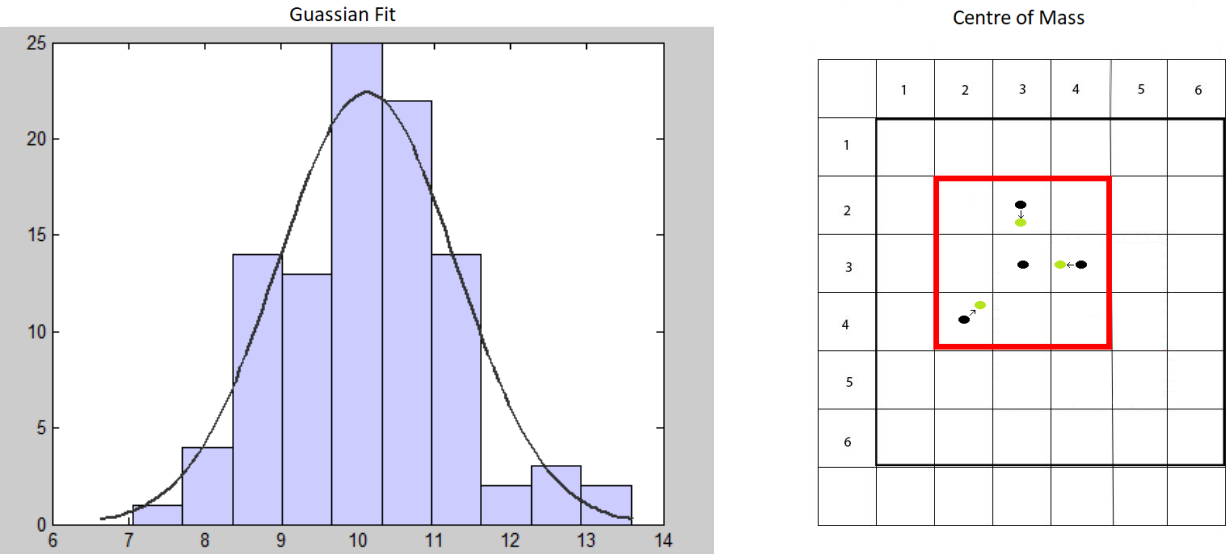


**Figure 9 Gaussian Fitting (Kennedy, 2013) versus Centre of Mass**

### 4.3.3 Center of Mass method

The relatively simpler COM method weighs each pixel with a group of pixels decided from the parameters of the ROI per its brightness to determine the centroid. Due to the reduced computational time required from the COM method, it was employed as the centroiding technique of choice to estimate the location of stars in the image plane to the sub-pixel level (Kandiyil, 2009; McBryde and Lightsey, 2012). The COM operation is implemented by using the rough estimate of the star's location from the threshold process. The ROI defined in the thresholding algorithm as mentioned above is centred over the brightest pixel, assumed to be the centre pixel of the star. The pixels that fall within the ROI are checked again to pass the threshold conditions. This ensures that only pixels with star light are used in the centroid calculation and not any pixels that fall below the brightness threshold. This feature was

implemented in the algorithm due to the results of the PSF as stars light disperse to a range of four to nine pixels on the sensor.

The output of the COM operation is a series of X and Y (subpixel accuracy) locations. These X and Y values are the estimated two dimensional coordinates of the star locations in Cartesian space on the image plane. The converted coordinates are used by the matching algorithm to find a pattern match between a star catalogue and the sensor image. The X and Y values are found by summing the product of the intensities and pixel locations as shown.

$$B = \sum_{i=1}^{3} \sum_{j=i}^{3} \tilde{I}(j,i) - n$$

$$X = \frac{\sum_{j=1}^{3} \sum_{i=1}^{3} \tilde{I}(j,i) * j - n}{B} + k$$

$$Y = \frac{\sum_{i=1}^{3} \sum_{j=i}^{3} \tilde{I}(j,i) * i - n}{B} + \ k$$

Where B is the intensity of the ROI with $n$ the noise threshold, $\tilde{I}(j,i)$ is the pixel intensity at location (j, i) with j being a column value and i being the row value, and k equal to 0.5 (The + 0.5 pixel is due to the x and y coordinate transformation to Cartesian values which has the value located at the corners of the pixel).

After the location of the stars had been estimated, the next step is to change coordinates from the image plane to that of the inertial frame. This was accomplished with moving the centre of the reference frame from the corner of the sensor to that of the centre of the sensor.

$$X = -X_o - \frac{R}{2}$$

$$Y = Y_o - \frac{C}{2}$$

Where X and Y represent the translation, with $X_o$ and $Y_o$ corresponding to the original frame coordinates and R and C are the amount totals of row and column pixels of the sensor. The negative in front of the Xo is due to the mirror image when flipping from the sensor frame. Once the frame has been adjusted, the stars are then projected from the x-y frame of the sensor to the unit vector of the celestial sphere. This adjustment is due to the shift of a two-dimensional image to a three dimensional, using the equation shown in page 108 (Huffman, 2006).

$$X_V = X_c * \left(\frac{P}{F}\right)^2 * \sqrt{1 + (X_c^2 + Y_c^2) * (\frac{P}{F})^2}$$

$$Y_V = Y_c * \left(\frac{P}{F}\right)^2 * \sqrt{1 + (X_c^2 + Y_c^2) * (\frac{P}{F})^2}$$

$$Z_V = \sqrt{1 + (X_c^2 + Y_c^2) * (\frac{P}{F})^2}$$

Where $X_c$ & $Y_c$ are, the centroid values represented in the image plane, F is the focal length of the optical system, P represents the pixel size and X, Y, and Z are in the inertial frame. This equation is based on the merit that the pixels are square pixels.

## 4.4 Star Identification Method

Star identification methods are required to determine the pointing position of the satellite as the FOV of a star camera is limited and too small to see entire constellations or large areas of the sky. A matching algorithm is implemented once the camera image has been converted to the inertial frame. Star recognition methods are implemented to cross-reference the centroided results of a star to that of the star in a catalogue. All the methods described in this section will utilize the unit vectors obtained from the centroiding stage. A set of variables is generated from the methods below that allow for a unique answer when searching the catalogue.

An optimal system capable of achieving the desired scientific outcomes often requires choosing a method by intercomparing the benefits and limitations of each different method. These method classes: subgraph isomorphism and pattern recognition (Luo et al., 2015). Each class can be broken down into several groups including polygon algorithms, grid algorithms, voting algorithms, neural network algorithms and genetic algorithms. A brief description of some of the more commonly used methods and their strengths and limitations is included in this section Methods such as the neural network and genetic algorithms will not be discussed as they require a large computing ability that nanosatellites currently cannot support (Luo et al., 2015; Spratling and Mortari, 2009). A large focus of this section is on the polygon methods, as these methods are implemented using geometry to determine a unique set of attributes that are compared to a reference catalogue. These methods are some of the earliest and computationally efficient methods.

### 4.4.1 Liebe Vector Angle Method

One of the earliest methods developed to solve the "Lost in Space" condition for attitude determination is based on Liebe's idea to used two inter-star angles and one interior angle (Spratling and Mortari, 2009). The angular distance between two neighbouring stars and a central star provided the inter-star angle. The interior angle is calculated through the use of the angle created between the three stars Figure 10 Vector Angle Method (Liebe, 1995). Liebe's method takes advantage of the unique angular patterns and does not require the use of the stellar magnitude values. The computational requirements for determining the angle between stars is very low due to the simplicity of this method. However, the reduced computational requirements are offset by potentially higher errors that arise from measurement noise that must be resolved in order to determine the correct angle. If the noise follows a Gaussian distribution, it can be

quantified using a standard deviation to determine the distribution (Cole and Crassidis, 2006).

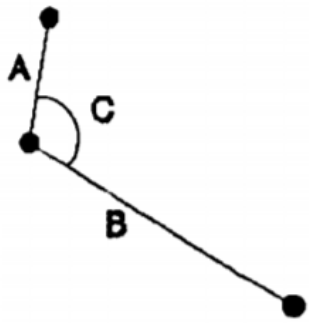


**Figure 10 Vector Angle Method (Liebe, 1995)**

### 4.4.2 Planar Moment Method

The planar method expanded on Liebe's Vector Angle method by implementing a third star. The third star allowed for the creation of a triangle which provided more information to be compared than the two-star system. The procedure of this method first determines the variables 'a', 'b' and 'c' show in Figure 11 Planar Moment Method (Diaz, 2006) by using the unit vectors $V_1$, $V_2$, and $V_3$ obtained through the calculations from the centroiding algorithm. $V_1$, $V_2$, and $V_3$ represent the vector from the origin to the respective star. While the variables 'a', 'b' and 'c' represent the slides of the planar triangle. Using these newly obtain variables it is possible to then calculate the planar angles of the triangle through the use of the Laws of Cosine thereby determining three angles $\emptyset_1$, $\emptyset_2$ and $\emptyset_3$. These planar angles are views the same in both the inertial frame as viewed in the body frame of the satellite. The following shows the equations needed for implementation of the planar moment method.

$$a = |V_1| - |V_2| \qquad \emptyset_1 = \arccos\left(\frac{a^2 - b^2 - c^2}{-2bc}\right)$$

$$b = |V_2| - |V_3| \qquad \emptyset_2 = \arccos\left(\frac{b^2 - a^2 - c^2}{-2ac}\right)$$

$$c = |V_1| - |V_3| \qquad \emptyset_3 = \arccos\left(\frac{c^2 - a^2 - b^2}{-2ab}\right)$$

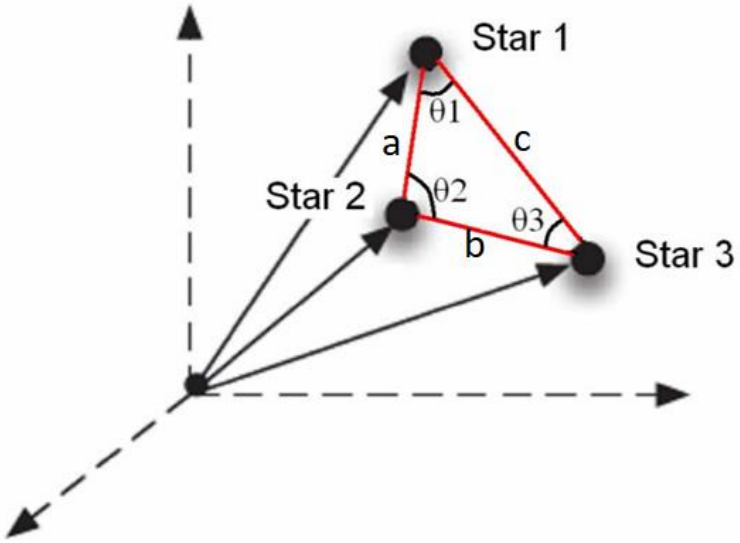


**Figure 11 Planar Moment Method (Diaz, 2006)**

### 4.4.3 Area and Polar Moment Method

The Area and Polar Moment Method changes the parameters to be compared from the image to the catalogue. This method continues to uses three stars to create a triangle in order to perform star identification. The use of the same variables 'a', 'b' and 'c' are calculated in the same way as in section 4.4.2 Planar Moment Method. The use of these variables then allow us to determine the area of the planar triangle by Heron's formula (Cole and Crassidis, 2006). The following shows the equations required to implement this method.

$$Area = \sqrt{s(s-a)(s-b)(s-c)}$$

where s is obtained using the variables 'a', 'b' and 'c'

$$s = \left(\frac{1}{2}(a + b + c)\right)$$

Since the area of two triangles can be the same a second parameter is required to present uniqueness to the search algorithm. Therefore, the calculation of the polar moment is also required. The polar moment is also calculated using the same variables as above.

$$Moment = Area * \frac{(a^2 + b^2 + c^2)}{36}$$

The red triangle in Figure 12 Polar and Area Moment Method (Diaz, 2006) indicates the region of interest for the area and polar moment calculation.

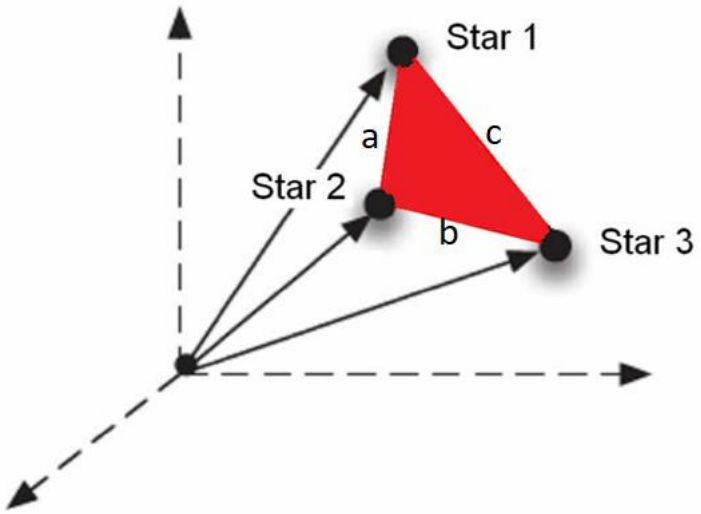


**Figure 12 Polar and Area Moment Method (Diaz, 2006)**

The original design of the polygon methods uses three observed stars to solve the identification process. However, if a star is misidentified because of an error there is no resilience to the identification algorithm. A false match leads to either an incorrect answer from the attitude determination or a re-selection of stars from the current or new image. Both increase time required to generate a correct star identification. Therefore, to reduce the likelihood of a false match, Mortari (Mortari et al., 1997) used a fourth star in the search process to increase the probability of a correct identification, called the Pyramid method.

### 4.4.4 Pyramid Method

The Pyramid method aims to produce a more accurate solution than the originally proposed triangle methods. This method builds on the basic triangle created from three stars and adds a fourth star to increase the probability of a correct match. These triangles are generated using the inter-star angles and require no information from the stars' brightness (Mortari et al., 1997).

A priori information regarding a previously viewed star is often required when only three stars are imaged as the knowledge of a previous star location is required to generate the fourth star. Alternatively, the method can incorporate the simpler triangle methods should no priori information be available. The problem remains that sparse regions in the sky can limit the number of visible stars. The Pyramid method can be adapted to work with the more complicated polygon methods (Area and polar method, Curve Angle method) (Mortari et al., 1997). However, due to the increase computational power required to perform these methods, the addition of a fourth star can significantly increase computing time required.

### 4.4.5 Novel Grid and Voting Methods

The grid method examines a whole image through the use of pattern recognition. (Padgett and Del Gado, 1997) Padgett *et al.* proposed the grid algorithm to solve the star identification problem by converting the pixels into strings of ones and zeros depending on pixels above a brightness threshold. In order to reduce the size of the matrix to increase computation, multiple pixels are merged together, which allowed for the algorithm to become insensitive to positional noise. However, this grouping of pixels also affects accuracy and reliability of the grid algorithm by decreasing the precision of the magnitude measurements. The grid method requires a large database to store the entire sky star pattern, which can be reduced in size with increasing the cell

to pixel size. This modified grid algorithm was proposed by Lee et al. and increases recognition accuracy compared to Padgett's original design (Luo et al., 2015).

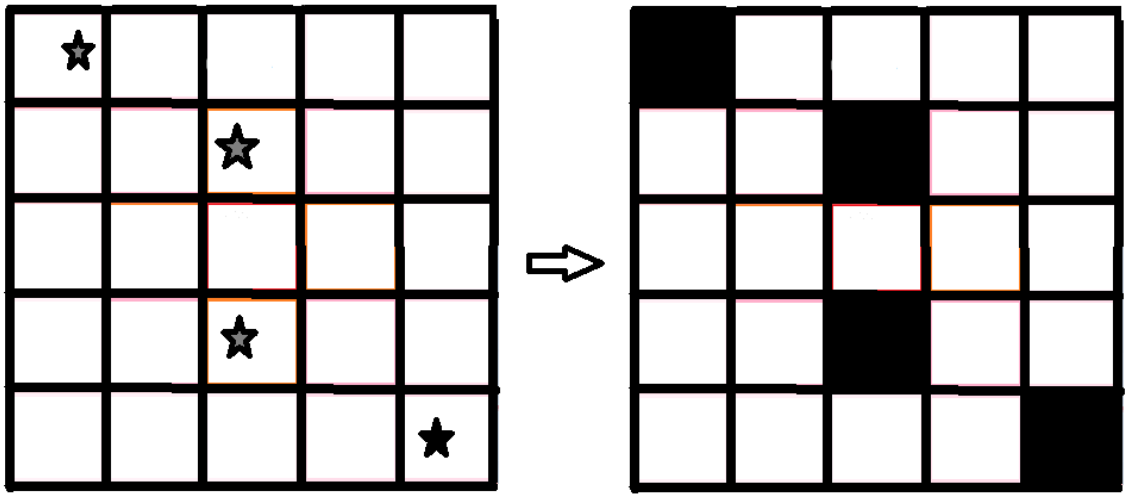

**Figure 13 Grid Method [Adapted from (Padgett and Del Gado, 1997)]**

The voting method matches the probability of occurrence of a star's appearance in an image by comparing stars to a catalogue. The algorithm first chooses a central star in the image, which is the main star for which all comparisons will be performed. The central star and one neighbouring star are selected and the angular distance between them is calculated. This angular distance is then compared with pairs of stars in a catalogue to find the matching pair. Once a matching pair is determined the stars' identification number is recorded. This process is repeated with the central star and its next adjacent star neighbour, until all stars in the image have gone through the process. The total number of appearances of a star results in the probability of that star being the correct candidate as the central star. An advantage of the voting method is that it does not use the magnitude values in its identification technique, reducing the probability of an incorrect match from sensor errors that improperly measured the intensity of star (Xie et al., 2012).

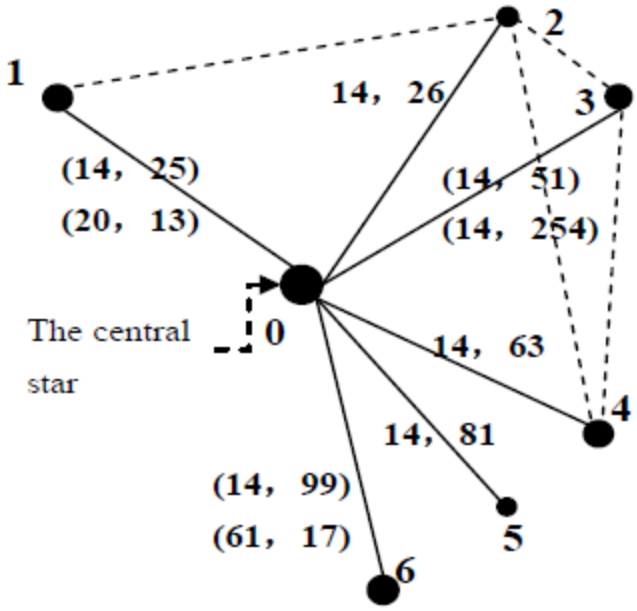


**Figure 14 Voting method: Central and Neighbouring Stars (Xie et al., 2012)**

## 4.5 Method Selection

In order to ensure optimal algorithm performance and ability to provide accurate attitude knowledge an intercomparison was performed between identification algorithms that focused on the important factors of computational power and the number of stars required. These factors limit the design options for this research to ensure simplicity of the algorithm to work in tandem with the provided hardware to perform the task in a reasonable timeframe. Since the provided hardware for the project was COTS components with a focus on low quality, the camera system cannot be relied on to provide optimal data for the algorithms over the lifespan of the mission. Therefore, the algorithm must be robust under different conditions in order to prevent capturing false stars due to atmospheric effects or even other satellites. Therefore, the magnitude of the stars was not used in a matching algorithm for this thesis as the optical system is expected to have a much higher chance of having components that will degrade faster than that of an

expensive (custom) camera system. This degrading of components will alter the information over time by causing distortions and errors.

The Grid methods as well as the Voting methods were not selected due the requirement of multiple stars in the FOV. Both methods require many stars in the captured image in order to accurately provide information for the identification methods. Testing of the COTS camera system indicates that the algorithm required for this research must operate with a minimal number of stars (<4) in a single frame. Only methods that are able to solve the identification problem with a maximum of four stars were considered as tests of the optics demonstrated that this was the maximum number of stars for the given FOV. The polygon methods were the main candidates for the project because of its combination of high computational efficiency of the methods and the capability to work effectively with three or four stars. The Area and Polar Moment method was chosen due to the increased amount of information required to obtain an identification match over the standard triangle method. The angle between any two stare may not produce a unique occurrence during the search algorithm, however, the area and polar moment of a triangle produces a unique solution to the search problem. This allows for a relatively simplistic design for our hardware to operate efficiently ensuring the correct match is determined.

## 4.6 Star Catalogue

The star catalogue is a database of known reference star information. These catalogues contain information about the stars' position including properties such as right ascension, and magnitude. There are a variety of catalogues available including the Hipparcos, Guide Star, and Bright Star catalogues. The catalogue used in this thesis is the Bright Star Catalogue (BSC) that has been revised by Harvard. This catalogue was implemented for the reference catalogue due to the limiting magnitudes the COTS camera system was capable of detecting, as the Hipparcos and

Guide Star catalogues are designed for large satellites that have star cameras that detect magnitudes dimmer than the visible eye can detect (Browse Software Development Team, 2012; Lasker et al., 1990). The BSC is also known as the Yale Bright Star Catalogue and contains stars of stellar magnitude 6.5 and brighter. The catalogue contains 9096 stars that are all visible by the naked eye (Warren Jr., 1991).

The BSC contains a large amount of data reducing the number of attributes in the BSC that are not required for the star identification algorithm a new modified catalogue is created specifically for this research. This new catalogue was referred to as the base catalogue. This catalogue was constructed based on the visible magnitude of the camera system through the use of a Monte Carlo analysis (Irvin, 2014). The first step was to limit the number of stars in the base catalogue using a list search that saves the information of stars that met the brightness threshold criteria. Once the selected stars were determined, a conversion from Spherical coordinates of the star catalogue to Cartesian coordinates in the inertial reference frame was performed. The conversion to Spherical coordinates required the conversion from degrees, minutes, and seconds to decimal degrees. After the first list of stars had been created a new list was required, the stars that pass the magnitude selection were then categorized into groups of stars that were visible within the FOV. This operation was performed using the equation below where the distance between the two stars are compared to the cosine value of the FOV.

$$Star1 \cdot Star2 \geq \mathrm{Cosd}(\mathrm{FOV})$$

Calculations of the pattern matching algorithm (Area and Polar Moment Method) concluded the tasks for creating the base catalogue.

The BSC was truncated for stellar magnitudes 4.0 (513 stars), 5.0 (1602 stars), and 6.0 (4800 stars) with a 31.8 degree FOV based on the design of the optical instrument. The modified

catalogue provides a sphere of detectible stars that matches the performance of the star imager's optics. The creation of the star catalogue is done separately from the main searching algorithm and is uploaded as a search list into the star camera algorithm.

Attributes taken from the BSC to create the modified catalogue include:

1. Harvard Revised Number: Number assigned to objects from 1 to 9110 in the catalogue
2. Hour: Right ascension for equinox J2000 and epoch 2000.0
3. Minutes: Right ascension for equinox J2000 and epoch 2000.0
4. Seconds: Right ascension for equinox J2000 and epoch 2000.0
5. Degrees: Declination for equinox J2000 and epoch 2000.0
6. Minutes: Declination for equinox J2000 and epoch 2000.0
7. Seconds: Declination for equinox J2000 and epoch 2000.0
8. Visual Magnitude: The apparent magnitude of an object as seen from Earth with the absence of an atmosphere (Used for limiting the catalogue size).

## 4.7 Attitude Determination

The attitude (or orientation) of an object is express using a coordinate frame. Within this coordinate frame a set of orthogonal axis is often used to described an object. This frame is often referred to as the body coordinate system. In order to describe the body coordinate system a determined reference system is required. This determined system is known as the inertial frame and provides the body frame with a set of values that have a meaningful origin. An example of this is an aircraft with its roll, pitch and yaw. While the roll, pitch and yaw describe the orientation of an aircraft they do not provide a facing to describe the directional path of the aircraft. An inertial frame is required to define the motion of the aircraft as travelling south. There is a rotation that expresses the set of coordinates of an object in the body frame to that of

the inertial frame. Therefore, the specific process of attitude determination is to determine the appropriate transformation to rotate from one coordinate system to the next (Sidi, 2000).

This algorithm uses all the information collected from the previous sections of the star imaging algorithm. The matching algorithm provides a list of vectors from the inertial coordinate system and the body frame. The inertial coordinates are selected from the reference catalogue of all the star locations while the body frame coordinates are the values determined via the centroiding process.

### 4.7.1 Attitude Determination Methods

The creation of attitude determination algorithms started with what was known as Wahba's problem in 1965 (Wahba, 1965). The problem started with two sets of vectors, whose components in the body and inertial frames are fully known. The next step was to determine a rotation operation between frames that the body set of coordinates were expressed through the inertial frame. Wahba's solution realizes that this problem may be solved as an optimization or search problem by minimizing the least squares residual. The problem lead to the use of a cost function to find an orthogonal matrix that minimized the loss function, shown below.

$$J(\boldsymbol{A}) = \frac{1}{2}\sum_{i=1}^{m} a_i \left|\left|\boldsymbol{b}_i - \boldsymbol{A}\boldsymbol{r}_i\right|\right|^2$$

Where J is the loss function, i is the observation number, m is the total number of coordinates, $\mathbf{a}_i$ are the weighted values, $\mathbf{b}_i$ is the body vector, $\mathbf{r}_i$ is the inertial vector and **A** is the chosen (or tested) orthogonal matrix. Once the residual **J** has been minimized, the associated matrix **A** is assumed to be the rotation matrix. Several different methods have been created to solve Wahba's problem since it was first introduced, some of these methods will be described in this section.

The TRIAD method solved the attitude problem using the Directional Cosine Matrix to rotate the vectors from the body and reference frame (Black, 1963). This method assumes that one given vector set is completely correct due to its use of only two vectors and therefore being underdetermined. The TRIAD method has been limited in the application of star imagers as a completely correct vector is not possible.

The development of methods using at least three vectors are separated into two groups: the robust and the computationally efficient methods. The tradeoff between robust and computationally efficient algorithms is taken into consideration for any system. For nanosatellites that have a small power budget and low computational abilities the tradeoff becomes a very important factor, a fast processing algorithm becomes a priority. The robust methods are the Davenport's q-method and the Singular Value Decomposition (SVD) method. The q-method was one of the earliest solutions developed. The q-method determines the solution using an optimal least-squares approach and as the name implies the SVD is determined for the methods solution (Delabie, 2016). However, since these methods are computationally slow at solving the attitude determination problem several other methods have been developed. QUaternion ESTimator (QUEST) was designed to solve the characteristic polynomial equation for the maximum eigenvalue of the Davenport Matrix K, thus allowing for the construction of the optimal attitude quaternion. The QUEST method with its estimation of the q-method parameter is computationally faster than the Davenport method at the cost of robustness. Increased computational efficient algorithms lead to the creations of Fast Optimal Attitude Matrix (FOAM), EStimator of the Optimal Quaternion (ESOQ) and Second EStimator of the Optimal Quaternion (ESOQ2).

The methods mentioned above have been tested against each other in (Markley and Mortari, 2000) with (Duarte et al., 2009) only comparing a couple of the above methods. These papers compared the performance of each method by looking at the number of operations a method uses, the number of observed vectors required to perform the operation as well as the standard comparison of the error in the attitude value calculated. These comparisons show a distinct separation between robust methods and computationally efficient. These two groups were plotted in figures (4) and (5) in "How to Estimate Attitude from Vector Observations" by F. Landis Markley and Deniele Mortari (Markley and Mortari, 2000). The plots indicate that the two slowest but most robust methods for solving Wahba's problem are the q method and the SVD. These methods minimize the loss function, where the loss function measures the discrepancy between the estimation and desired output. When the required number of observed vectors is greater than three the q method maintains an edge in computation time over the SVD method. Faster algorithms are less robust as they solve the characteristic polynomial equation to find a maximum eigenvalue to the K matrix from Davenport's q method but with the limitation of reduced accuracy for attitude determination. Although the fastest methods are all very close to each other in the number of operations performed, FOAM is the most robust of the fast methods while ESOQ and ESOQ2 are the fastest overall methods.

Therefore, the algorithms from figure (5) in "How to Estimate Attitude from Vector Observations" were determined to be the best suited for the research and the star imager system. From these computationally faster algorithms QUEST was decided as the method of choice. QUEST performs slightly slower then methods such as ESOQ and ESOQ2 but due to its ease of implementation, its relative robustness and high performance it is well suited for the attitude determination on nanosatellites (Huffman, 2006).

### 4.7.2 QUEST algorithm

The following method was implemented in "Improvement to the Implementation of the QUEST Algorithm" (Cheng and Shuster, 2014). The QUEST method is based on the property that $\lambda_{max}$ is easily obtained by a Newton-Raphson iteration with the starting condition of $\lambda_0$ is equal to one. The implementation of QUEST uses two sets of unit vectors to determine the attitude of the satellite. This is accomplished with one set of vectors derived from the image of the camera system, while the other set of vectors are supplied from the star catalogue. Using these sets of vectors the characteristic polynomial equation is estimated to provide the optimal quaternion.

The following equations show the steps that were taken to implement the QUEST algorithm. The first step is to rewrite wahba's problem in the form of the loss function seen below.

$$J(A) = \lambda_0 - trace(AB^T)$$

Where $\lambda_0 = \sum_{i=1}^{m} a_i = 1$ corresponds to the initial condition, **A** is the orthogonal matrix and **B** is the attitude profile matrix represented by $B = \sum_{i=1}^{m} a_i b_i r_i^T$ where $a_i$ is weighted values usually inversely proportional to the measured noise variance, with $b_i$ and $r_i$ representing the unit vectors from the camera and catalogue. It can be seen that the loss function above is minimized when the $trace(AB^T)$ is maximized. The attitude matrix can also be parameterized by a unit quaternion as show

$$trace(AB^T) = q^T K q$$

Here **K** is symmetric traceless matrix

$$K = \begin{bmatrix} S - \sigma I & Z \\ Z^T & \sigma \end{bmatrix}$$

With elements,

$$S = B + B^T \qquad \sigma = tr[B]$$

$$Z = [-B_{32}, B_{31} - B_{13}, B_{12} - B_{21}]^T$$

The steps taken to this point are the same used in the Davenport q-method to obtain the **K** matrix. The next step in the implementation is all unique to the QUEST method. The characteristic equation is a fourth order polynomial function which is used to obtain $\lambda_{max}$.

$$\psi(\lambda) = \det(\lambda I_{4x4} - K) = 0$$

The characteristic polynomial equation can be expanded into the form show below

$$\psi QUEST(\lambda) = \lambda^4 - (a+b)\lambda^2 - c\lambda + (ab + cs - d)$$

With coefficients

$$a = \sigma^2 - trace\big(adj(S)\big) \qquad b = \sigma^2 + z^T z$$

$$c = \det(S) + z^T S z = 8\det(B) \qquad d = z^T S^2 z$$

The coefficients for the expanded characteristic polynomial are all functions of the elements from the **B** and **K** matrix. Subsituting the factored polynomial equation into the Newton-Raphson Iterative equation $\lambda_{max}$ can be obtained

$$\lambda_{max}^{(k+1)} = \lambda_{max}^{(k)} - \frac{\psi QUEST - fac(\lambda_{max}^{(k)})}{\psi' QUEST - fac(\lambda_{max}^{(k)})}$$

where $\psi' QUEST - fac$ is the derivative of $\psi QUEST - fac(\lambda)$ with respect to $\lambda$. The final solution is to obtain the optimal quaternion which is contstructed using

$$q_{opt} = \frac{1}{sqrt\left(\gamma^2 + ||x||^2\right)}$$

With coefficients that are again from the **B** or **K** matrix

$$\alpha = \lambda_{max}^2 - \sigma^2 + trace\big(adj(S)\big) = \lambda_{max}^2 - a$$

$$\gamma = \alpha(\lambda_{max} + \sigma) - \det(S) \qquad x = [\alpha I_{3x3} + (\lambda_{max} - \sigma)S + S^2]z$$

# Chapter Five: Camera Hardware Calibration Tests

The camera hardware requires several different calibration tests in order to characterise its performance. These calibrations ensure that the system is operating within an expected performance range and can mitigate errors through the use of a calibration map. Calibration maps are determined characteristics from the calibration procedure that are implemented to mitigate any errors or distortions measured. These tests are used to estimate the intrinsic and extrinsic parameters of the system. Intrinsic parameters refer to properties of the camera such as its focal length and principle point. Extrinsic parameters encompass the coordinate transformations of the planetary frame to the camera frame. Calibrating the system requires methods to estimate the lens and sensor characteristics individually as each component will have its own performance bench mark. The calibrations conducted during this research are (1) checker board, (2) flat field, (3) point spread and (4) hotspot tests. Procedures and results from each test are described in this chapter. Dark current was the only temporal noise addressed in this research as many temporal sources are beyond the scope of this research.

**Figure 15 Calibration Table Setup**

## 5.1 Checker Board Calibration Procedure

The Checker Board test is designed to estimate the intrinsic characteristics of the camera, including focal length, skew, distortion, and principle point. This test compares the camera's apparent dimensions of a spatial pattern in the (distorted) image output to the known dimensions of the pattern. A checkerboard pattern is often used for its straight edges and easily distinguished components.

A black chamber was constructed for the calibration tests Figure 15 Calibration Table Setup in order to minimize both the light emitted from the FPGA board and stray (ambient) light. Providing dark environment for the test facility is important during calibration because a homogeneous light source and any stray light will create signal that is uncharacterized and therefore impossible to correct for. Several conditions were implemented to ensure a successful calibration. The autofocus feature on the camera was turned off, ensuring that the focal length remained the same. To obtain a clear image of the pattern diffused light from the source was used and extreme angles of the checker board pattern were avoided (Zhang, 1999). The calibration procedure used a Camera Calibration Toolbox (MATLAB toolbox), developed at the California Institute of Technology. The toolbox offers several methods for performing various calibration procedures and its simplistic implementation made it a viable option for this research (Bouguet, 2015).

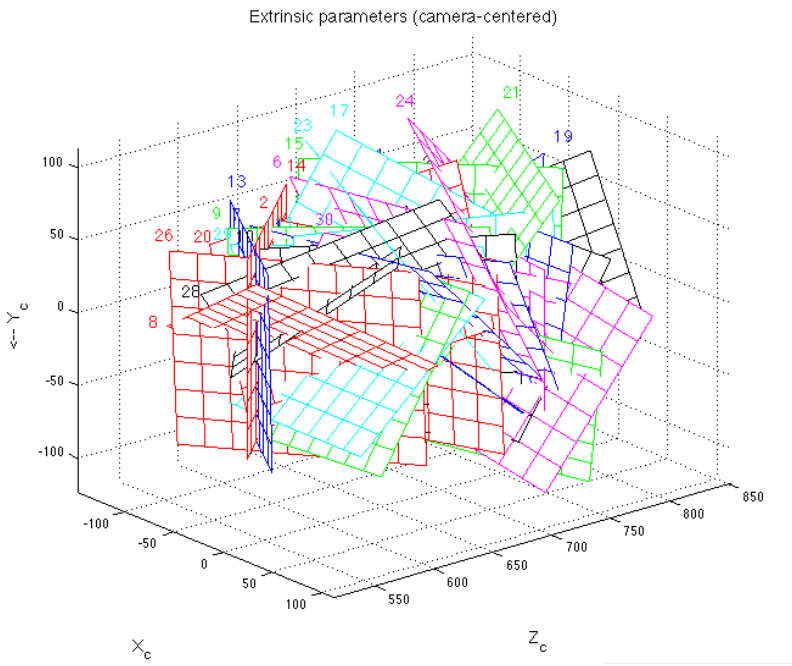


**Figure 16 3-dimensional Visualization of Orientations**

A black and white checker board pattern was mounted onto a flat surface at a distance that ensured that the entire pattern was contained within the camera's FOV by accounting for the camera's focal length. A flat surface is provided in this calibration as any distortion on the surface will appear as a distorted checkered pattern, which introduces uncertainties into the test results. 30 images were taken of the pattern in different orientations (rotations within xyz space) and at different locations in the vertical plane throughout the FOV. Several images at various positions and orientations are required in order to determine the average error for the entire lens system. If only one image was taken, the estimated error would be representative of patterns at specific (not all) locations within the FOV. A sufficient number of distributions and orientations ideally ensure that the estimated residual error is representative for the entire sensing area. Once enough images have been collected, the outer edge corners of the checker board pattern are manually selected for the toolbox from each image. Selection of the corners ensures that the

toolbox can correctly determine the patterns' positions and shapes. The dimensions of the checker board squares must also be uploaded to the toolbox. The program then calculates the number of squares in each direction.

The calibration procedure first conducted an initialization, to calculate the camera parameters without any lens distortion, and then a least-squares optimization that minimizes the error in the reprojection of the corners using the calibration parameters. The toolbox includes the option of corrections in the corner selections as well as just replacing lower quality images with better ones. By retaining only good quality images, the accuracy of the calibration results is improved.

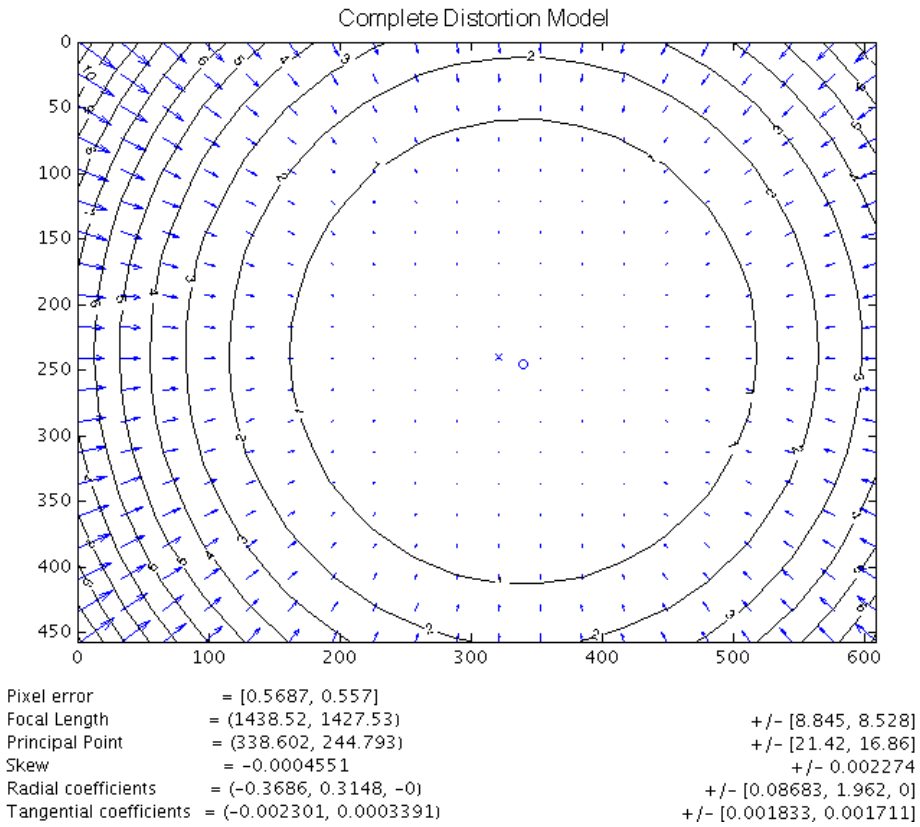


**Figure 17 Camera Calibration Toolbox Complete Distortion Model**

## 5.2 Results of Checker Board Calibration

The output from the calibration toolbox is displayed using a distortion model depicted in Figure 17 Camera Calibration Toolbox Complete Distortion Model, that provides information on most common parameters from the calibration procedure, including the pixel error, focal length, principal point, skew, radial coefficients and tangential coefficients. The distortion model provides an estimated pixel error for the images collected. This estimated error suggests that objects imaged will be out of place by this error in pixel space. This pixel error is calculated from the reprojection error over all the images in the calibration set and resulted in a standard deviation of 0.569 in the x and 0.557 in the y directions.

The calculated focal length from the calibration procedure is also given in the x and y coordinates with dimensions in pixels. This value can be multiplied by the pixel size to calculate the focal length of the camera in SI units. The pixel size of the sensor array is 6µm by 6µm and results in the calculated focal length of 8.63mm±0.05mm in the x direction and 8.56m±0.05mm in the y direction. The x and y focal length values are similar as the pixel array of the sensor has square pixels. The results of the focal length calculation compared very well to the manufactures value of 8.5mm; this slight difference between the actual and calculated value would suggest that the images acquired were slightly defocused during the test.

The principal point is also given in units of pixels and represents the origin of the distortions. The MATLAB script marks the principal point by using a ‘o’ and the centre of the image is marked with an ‘x’. The differences in these values show that the distortions are not aligned with the central axis of the sensor (The ‘x’ and ‘o’ are displaced from each other). The incorrect alignment can originate from two sources. The first is the construction of the CMOS pixels since the sensors’ pixels are square in shape but the active region only covers $3/4^{th}$ of this

pixel while the rest of the pixels' surface is components for its operation. The second is due to the alignment of the sensor under the bore sight since a misalignment of the optical system with the sensor may cause the shift in the principle point. The offset of the principle point from the centre of the sensor is visible in the left side of Figure 17 Camera Calibration Toolbox Complete Distortion Model as the maximum values (arrows on image) of the distortion map are skewed towards this side showing an uneven distortion pattern.

The last two parameters determined from the checker board calibration are the radial and tangential distortion coefficients with the tangential component (-0.0023, 0.0003) being considerably smaller than that of the radial component (-0.3686, 0.3148, 0.0000). The tangential component only has two values as it is described in terms of sinusoidal values in polar coordinates along the u and v axis whereas the radial values are described in the Cartesian coordinates. The large difference between the tangential and radial components is likely due to the manufacturing of the lens system, as tangential distortions are produced by the imperfections in alignment of the lens components and manufacture defects. The radial component of the distortion is generated from aberrations of the lens itself including distortion, astigmatism, field curvatures, and lens coma.

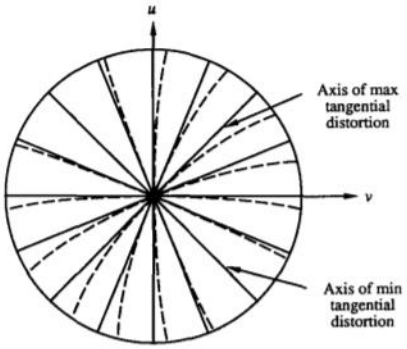


Fig. 4. Effect of tangential distortion. Solid lines: no distortion; dashed lines: with tangential distortion.

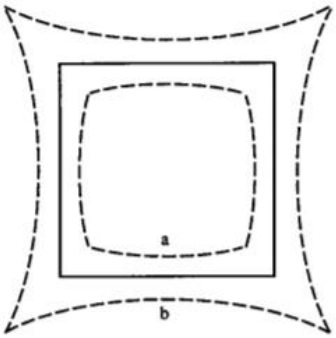


Fig. 3. Effect of radial distortion. Solid lines: no distortion; dashed lines: with radial distortion (a: negative, b: positive).

**Figure 18 Tangential and Radial Distortion Models (Weng et al., 1992)**

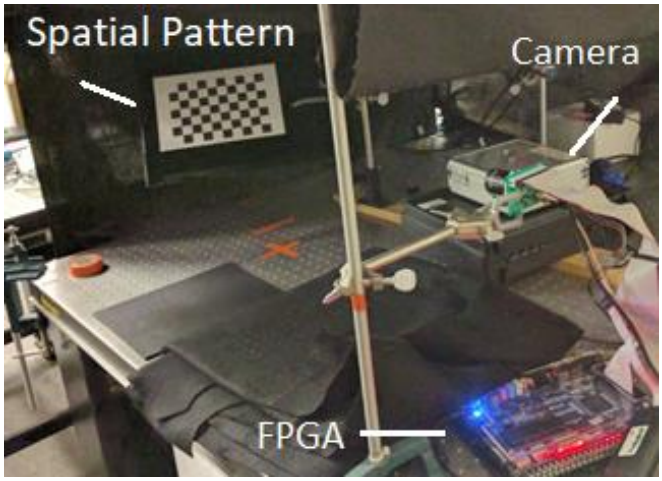


**Figure 19 Flat Field Calibration Setup**

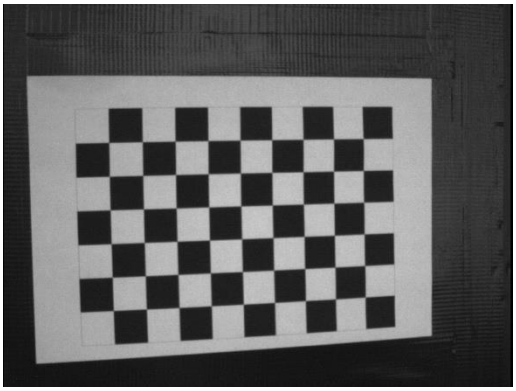

**Figure 20 Spatial Pattern Used During Calibration**

## 5.3 Flat Field Calibration

The flat field illumination calibration was performed to correct for the slight differences in the sensitivity of each pixel of the sensor to incident photons, known as Photo Response Non-Uniformity (PRNU). The PRNU describes the ratio between optical power incident on the pixel and its generated electrical signal output (Knight et al., 2009). The flat field image displays the fix pattern noise (FPN) as a non-uniform pixel readout shown in Figure 21 FPN from Flat Field Calibration.

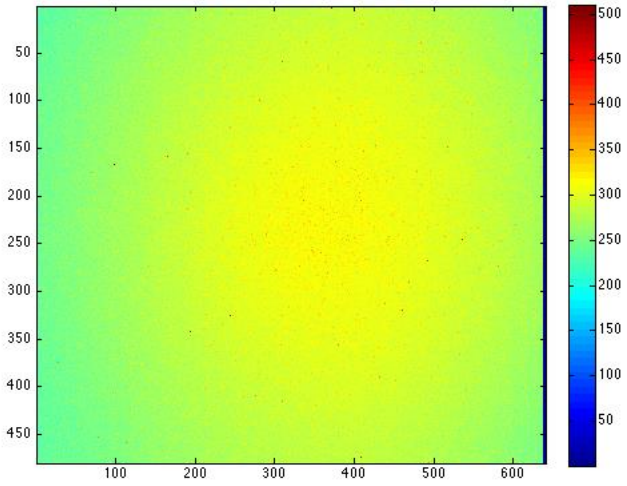


**Figure 21 FPN from Flat Field Calibration**

These differences in sensitivity add an additional noise component it requires a calibration map to adjust for the discrepancies. Flat field tests are also used to determine the vignette in the optical system. Vignette is a reduction in the amount of flux that arrives at the corners of the sensor compared to its centre (Catrysse et al., 2000). Figure 22 Normal versus Oblique Angle of Incident Light illustrates that when the incident light source is parallel to the pixel, the light will converge on a single pixel. However, at the corners of the sensor where the angle of incidence is highest, some of the incoming photons impact adjacent pixels. These impacts to adjacent pixels degrade the quality of the image as the signal is dispersed. Reducing vignette is possible by

increasing the focal ratio of the system, which uses vignette to intentionally prevent photons from entering other pixels. This method is not always viable as some systems lack the financial resources or space available in the system to increase component size to increase the focal ratio.

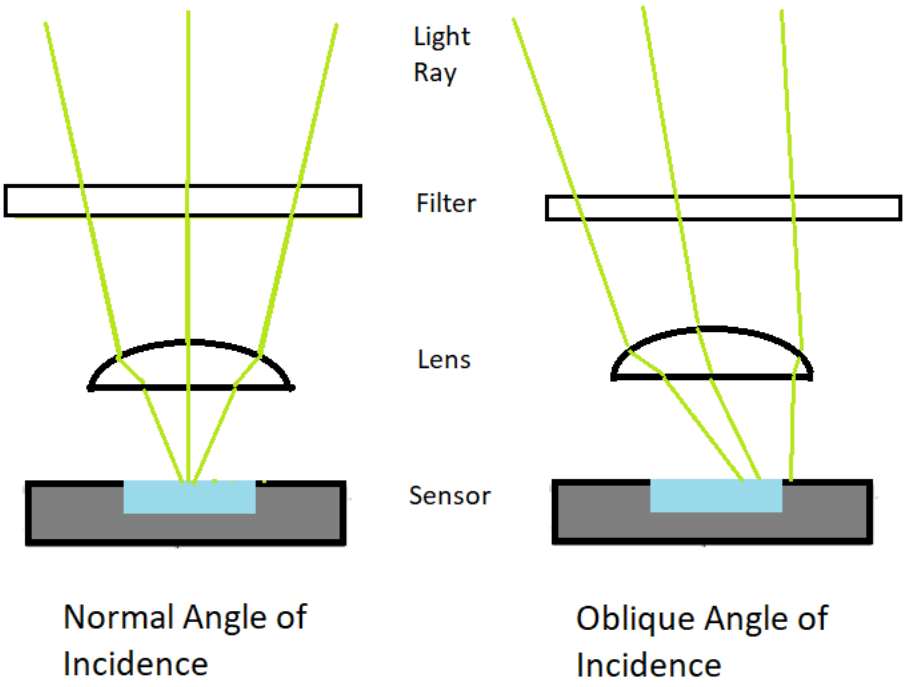


**Figure 22 Normal versus Oblique Angle of Incident Light**

For the flat field calibration, a Thor Labs SLS201/M light source with Neutral Density filters of value ND 1.0, 0.4 and 0.3 were used. The maximum value of the pixel intensity was ~ 50% with mean value of ~ 30%. This lower intensity level was used to ensure that the pixels would not become saturated and that measurements of the flat field were focused on the properties of the pixels during dim light. There are several factors that should be addressed while performing this calibration. Dust must be removed from the lenses since the presence of dust can produce a shadow on the sensor, affecting the uniformity illuminated surface. It is also important

to ensure that illumination levels remain stable as changing illumination levels changes affect the colour temperature of the light source.

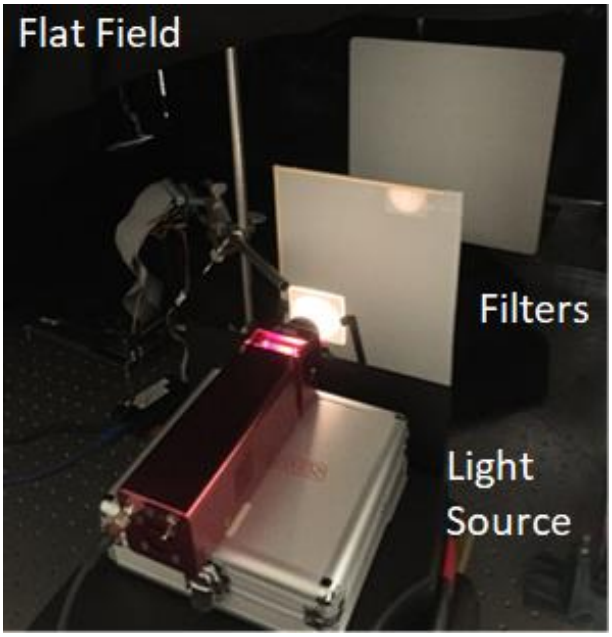


**Figure 23 Flat Field Calibration Setup**

The flat field calibration procedure starts with exposing the sensor to a uniform light source, either using a collimated source or a lambertian surface. A lambertain surface is often used to ensure that the same brightness is viewed from all angles due to the Lambets Cosine Law (Smith, 2000). In order to increase the effectiveness of the Lambertian surface, two opal diffusers were also placed in front of the light source. This diffusion of light ensured that our Lambertian surface was illuminated with an even point spread. A saturation of pixel sensitivity of 30% - 60% is required in order to reduce non-linearity and noise (Koene, 2016). This range is used for dark imaging as a brighter image will result in a loss of sensitivity. Dark current occurs when no signal enters the sensor, resulting in an image that is only affected by the small amounts of electrical current that flow through the photosensitive devices, even when no photons are entering the device (Porter et al., 2008). Similar to the checker board calibration, a set of 30

images of the light source were taken as well as approximately the same number of dark frame images (increasing the number of photos taken helps with weighing the averages). Each set of images (dark and light) had the average frame value calculated for all the pixels, normalizing this value across all images. The normalized values were then applied to the individual pixel values, thus adjusting the sensor readout to account for bias in sensitivity of each individual pixel. If a pixel is recorded as more sensitive than the average, it is assigned a value below one to adjust for its increased sensitivity. The same process is followed for pixels that are less sensitive, receiving a value above one in this case. Averaging of the pixel values across the sensor allows for the removal of the temporal noise that is minimized by the technological design of the sensor but never completely removed.

$$\overline{P_{ij}} = \frac{\sum_{k=1}^{N} P_{ij}^{k} P_{ij}}{N}$$

Where N = # images, Pij average value of pixel over all frames, and ij are row and Col

$$\bar{P} = \frac{\sum_{k=1}^{N} \sum_{i=1}^{C} \sum_{j=1}^{R} P_{ij}}{NCR}$$

P is average pixel across all frames, C is # of Col and R is # of Rows in frame.

$$FPN_{ij} = \overline{P_{ij}} - \bar{P}$$

## 5.4 Shutter Closed – Extension of the flat field test

The shutter closed calibration is used to determine the Dark Noise and DSNU of the sensor. DSNU is a parameter of FPN and describes the non-uniformity of pixel readouts when imaging a uniform scene, in this case a frame with no illumination (described in detail in chapter three “Noise and Aberrations Background”). The resulting noise generated from the current

flowing within the sensor is often referred to as a ‘hot pixels’ as the signal may be well above the average of the frame. These hot pixels can potentially interfere with the star detection algorithm that uses the brightness of the pixels to determine a stars’ location because the addition of the hot pixel values can skew the location of a stars measured position.

The closed shutter calibration uses the same method as the flat field test to obtain dark frames. Twenty images were captured for this calibration due to the convergence towards a single, consistent hot pixel value at this image sample size. A hot pixel was classified as any pixel that deviates from the average of the scene by more than five standard deviations from the means. The images collected during the process had to meet much of the same criteria that was implemented during the flat field calibrations. This includes no illumination occurring on the sensor and that hot pixels in the system minimized by maintaining a constant temperature on the sensor and exposure time. The importance of maintaining a constant temperature during the calibration is due to the intrinsic properties of electrical components that emit more electrons at higher temperatures. Therefore, a characterization of the sensor is possible by keeping the temperature constant and changing the exposure times of the sensor. Three exposure times were used at 480, 960, and 1140 rows of continuous readout and the associated times were 0.0243s, 0.0486s and 0.0729s. These readouts were chosen as they refer to the amount of time to read a single frame up to three frames. Calculating the exposure time of the camera was accomplished using the equation below.

$$t_{int} = N_{rows} x t_{row} + t_{overhead}$$

Where, $N_{rows}$ is number of rows being integrated across, $t_{row}$ is the integration time of the row, and $t_{overhead}$ is a camera characteristic inherent specifically to this camera, that is the extra amount of time required to process each image.

The test was performed with AEC (Automatic Exposure Control) and AGC (Automatic Gain Control) disabled, the results are shown in the table below.

**Table 5 Hot Pixel Test Results (AEC and AGC Turned OFF)**

| Exposure Time (Rows) | 480 | 960 | 1440 |
|---|---|---|---|
| Exposure Time (Sec) | 0.0243 | 0.0486 | 0.0729 |
| Number of Hot Pixels | 24 | 149 | 318 |
| Average Scene Value (0-1023) | 64.5 | 65.3 | 66.3 |

The results table above show the effect of dark current (temporal noise) on the sensor, by increasing the exposure time of the system. The hot pixels gradually increase in occurrence with the increased exposure. Only 24 pixels were recorded as hot pixels during the span of a 'normal' readout duration, while 318 pixels were recorded in a time span that was three times longer. This shows a 1325% increase in the number of recorded hot pixels.

## 5.5 Point Spread Function Test

The PSF is a characterization test used to determine the system's pixel response to a single, infinite point source. The PSF provides the distribution of the sensor readout information that is used in designing the centroiding algorithm. A star is defined by the system response of the PSF the clustering of pixels. In a perfect system, the PSF of a single infinite point source will appear the same size in the image plane. This means that if a pixel sized point source is used, only a single pixel would be illuminated. However, in reality, the point source will be distributed across a larger range due to the optical properties of the lens system. This concept of PSF illustrated in Figure 24 Ideal PSF where the ideal signal is concentrated on a single pixel, with the red regions indicating the brightest signal intensity and the blue regions showing the lowest

signal (close to background noise levels). Its real representation is approximated by a normal distribution. This distribution can have either an isotropic or non-isotropic shape, depending on the system. The PSF is also used in determining the minimum signal the sensor is capable of measuring with a specific pattern. Decreasing the point source power until the side peaks of the displayed signal just pass the centroiding criteria will determine the minimum signal strength required for the camera.

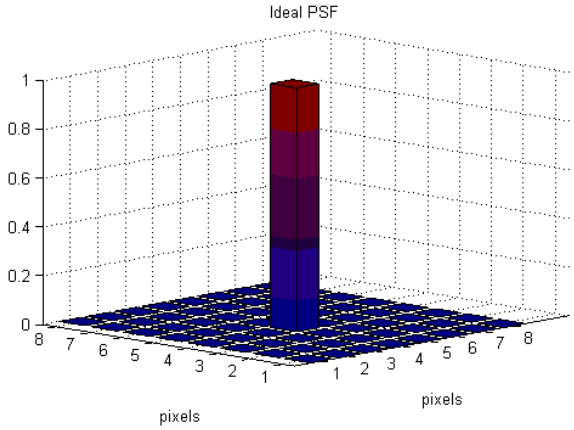


**Figure 24 Ideal PSF**

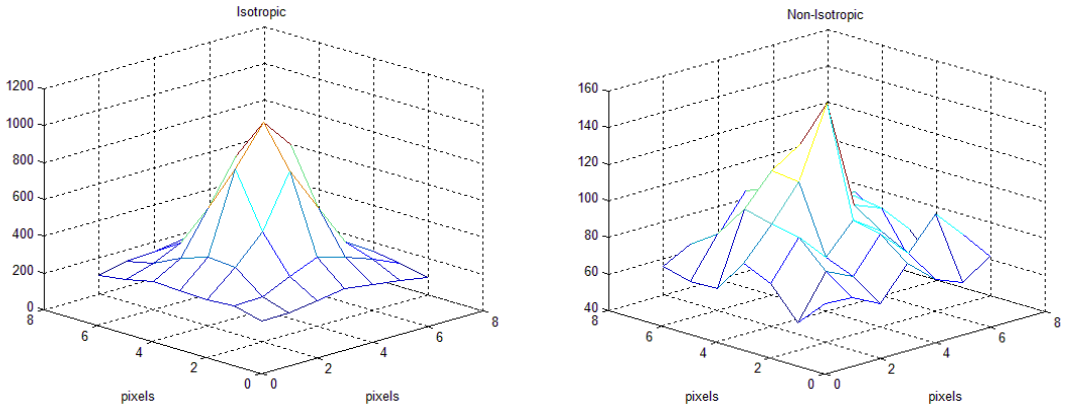


**Figure 25 Isotropic and Non-Isotropic PSF**

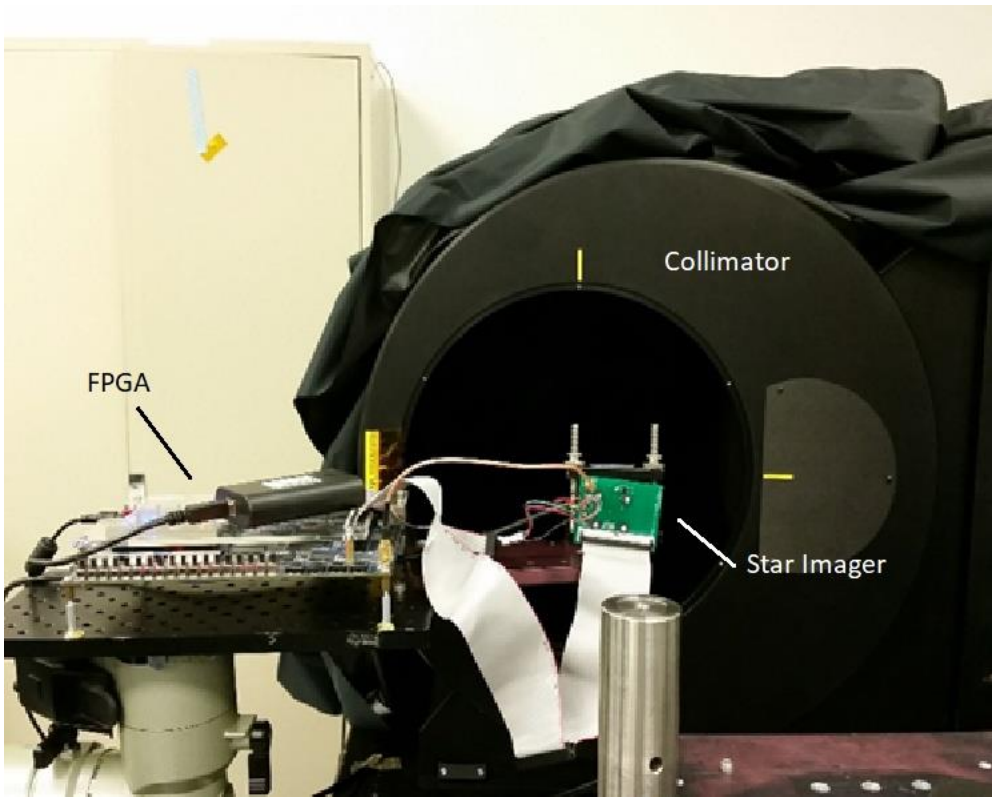


**Figure 26 PSF Calibration Setup**

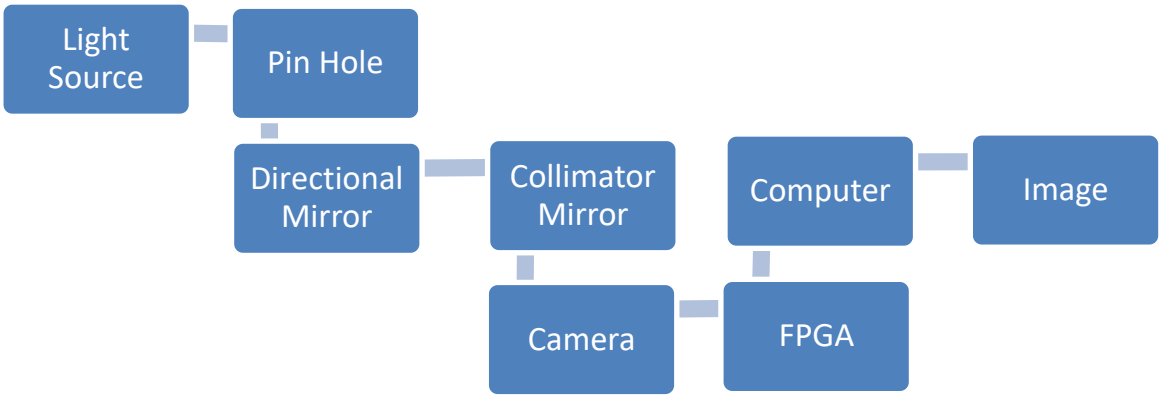


**Figure 27 PSF Calibration Flow Chart**

The entire PSF setup can be seen in Figure 26 PSF Calibration Setup with a flow chart describing the steps in Figure 27 PSF Calibration Flow Chart used to achieve the images conducted during this research. The camera was positioned on a tripod stage and placed in the middle of the entrance of the collimating system. A 0.002-inch pin hole was placed in front of a

broadband light source that reflected the light down a 60-inch collimating tunnel. The light from the collimating mirror at the end of the tunnel bounces the light back along the path of the collimator body out towards the entrance where the camera was positioned. The entire setup is covered with a dark cloth in order to minimize ambient light from entering the camera's sensor.

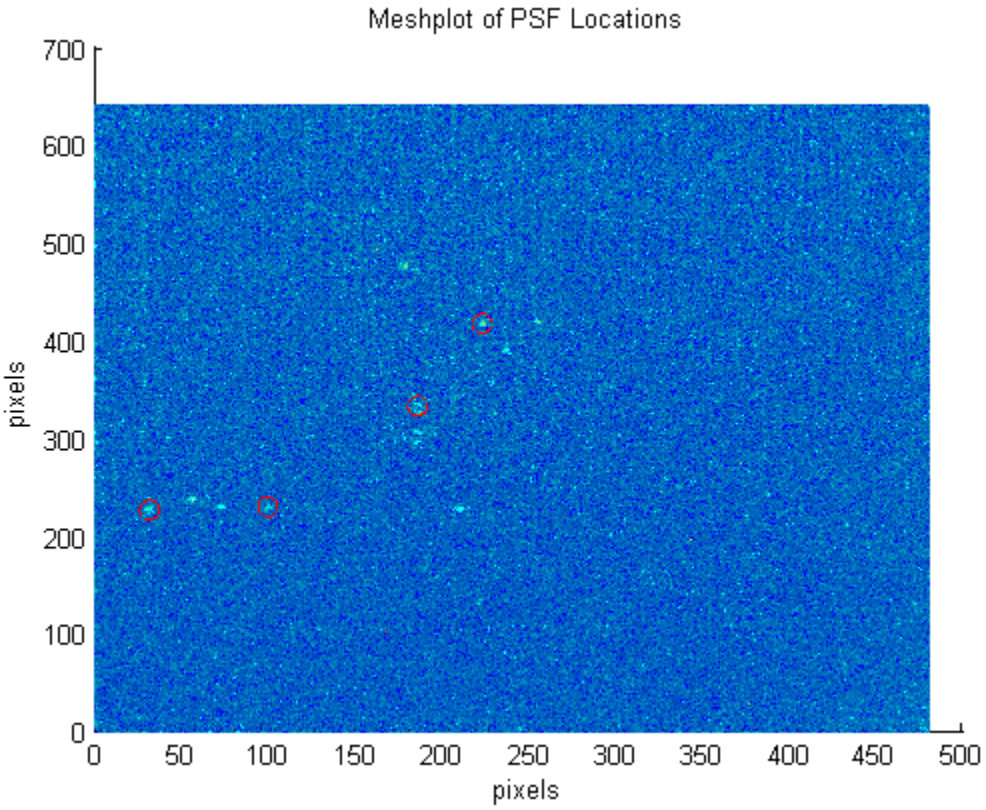


**Figure 28 Test Locations of PSF Calibration**

Figure 28 Test Locations of PSF Calibration shows the combined images of all the PSF test images and the positions of the point source on the sensing frame. Several images were collected at multiple locations on the sensor as the lens system will have contributed to different deformations across the lens due to manufacturing procedures. The importance of this screening is to properly measure the signal throughout the entire sensing area. Figure 29 PSF from Centre to Edge of Sensor (Side View) shows the PSF at four locations across the sensor (red circles in Figure 28 Test Locations of PSF Calibration); these images were selected to illustrate the PSF as

you move across the middle of the sensor towards an edge (Locations from middle towards edge 23, 9, 15, 18). Location 23 illustrates the PSF in the form of an isotropic distribution. The central column contains the majority of the signal while the adjacent pixels around this column have the next highest amount of signal. Locations 9 and 15 demonstrate the loss of the isotropic distribution (visible in the overhead views Figure 30 PSF from Centre to Edge of Sensor (Top View)). The overhead views of these locations no longer show a symmetrically looking pattern. Location 18 (closest PSF near the edge of sensor) demonstrates the case where the lens imperfections affect the shape of the collected signal as the PSF no longer maintains it structure (non-isotropic distribution).

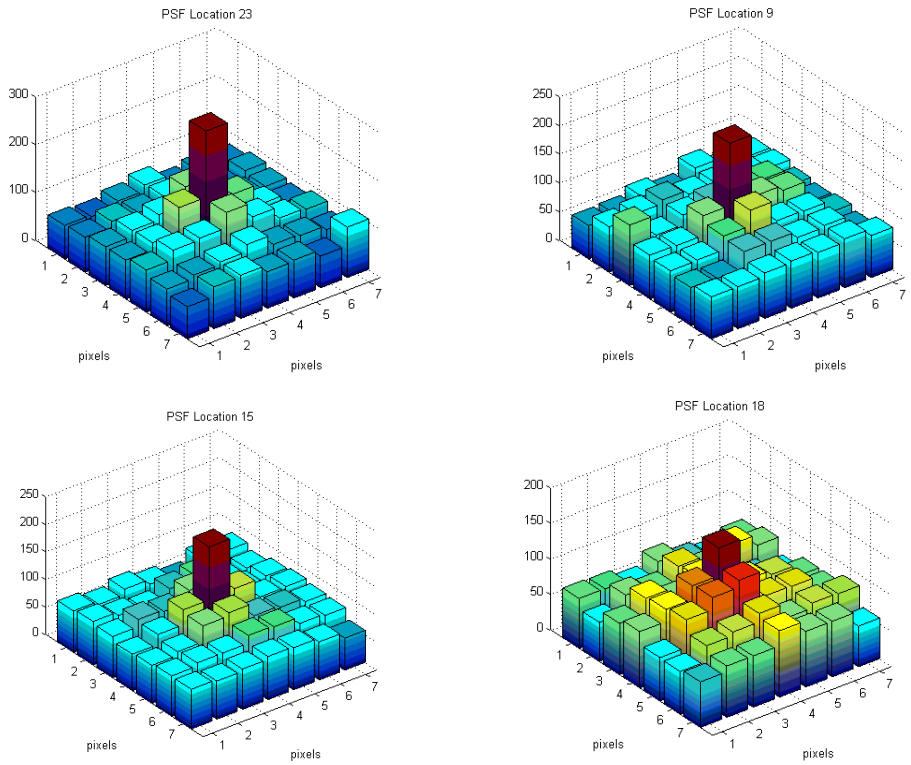


**Figure 29 PSF from Centre to Edge of Sensor (Side View)**

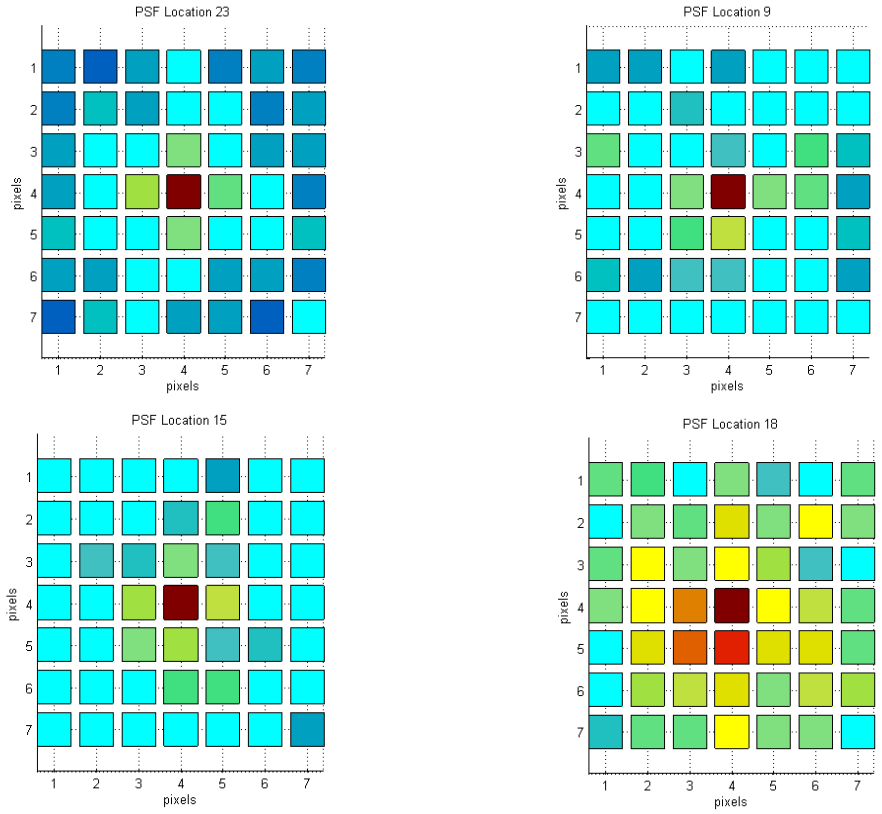


**Figure 30 PSF from Centre to Edge of Sensor (Top View)**

The images of the PSF indicate that the majority of the signal is located on the central pixel with some energy illuminating the nearest pixels in a '+'-shaped pattern. This degree of displacement of the signal is acceptable for this research as specified in the centroiding algorithm construction (chapter 4) where a minimum of four pixels are required to be checked to pass the criteria in order to be classified as a star. The pattern of light displaced on the pixels is a combination of the lens and sensor setup and this system can be adjusted by defocusing the lens to increase the spread across a greater region. This spread of signal will decrease the peak intensity in the central pixel and will increase the illumination of neighbouring pixels.

# Chapter Six: Simulations, Field Work and Final Results

## 6.1 Simulation

In order to examine the feasibility of the proposed CMOS camera hardware for star imaging several tests were performed including a full suite of simulation analysis on the centroid algorithm and the correlation to the identification and attitude determination methods. Several images from the field tests were also analyzed to validate the results predicted from the simulation study. The simulation test results as well as the discussion from the field work are described in this chapter.

### 6.1.1 Centroid Algorithm Simulation

The star camera algorithm was characterized through various methods that measured the functionality of the camera system through simulated data and a field campaign. The simulated data was designed to demonstrate the algorithm functionality. In order to verify the centroiding algorithm, star field images were generated with Stellarium open source software that projects the stars' coordinates in 3D creating a planetarium for the user. The simulated images were processed by the centroiding algorithm to determine the estimated star locations. The algorithm produced a list of centroid locations that was compared to the number of stars presented within the image, ensuring that the same number of centroids matched the number of stars. In the example image shown in Figure 31 Simulated Image with Centroid Locations, estimated star locations were achieved throughout the image. The centroiding algorithm estimates a star's locations based on the PSF that was implemented. This research implements a PSF that is a nine-pixel square, stars that fall within this bounds are correctly estimated. The image also contains two stellar objects that do not meet the star criteria (bottom middle of image near 1400-pixel

count). These stellar objects were also estimated by the centroiding algorithm. The two objects are considered false stars by the star imager algorithm and the robustness of the identification algorithm is required to determine a correct match to the catalogue without these objects causing any interruptions. There is also a single star in the top middle of the image which is also estimated by the centroiding algorithm, when a star is too close to the edge of the image it will not be used for the star imager algorithm as the PSF of this star has a higher probability of a distortion.

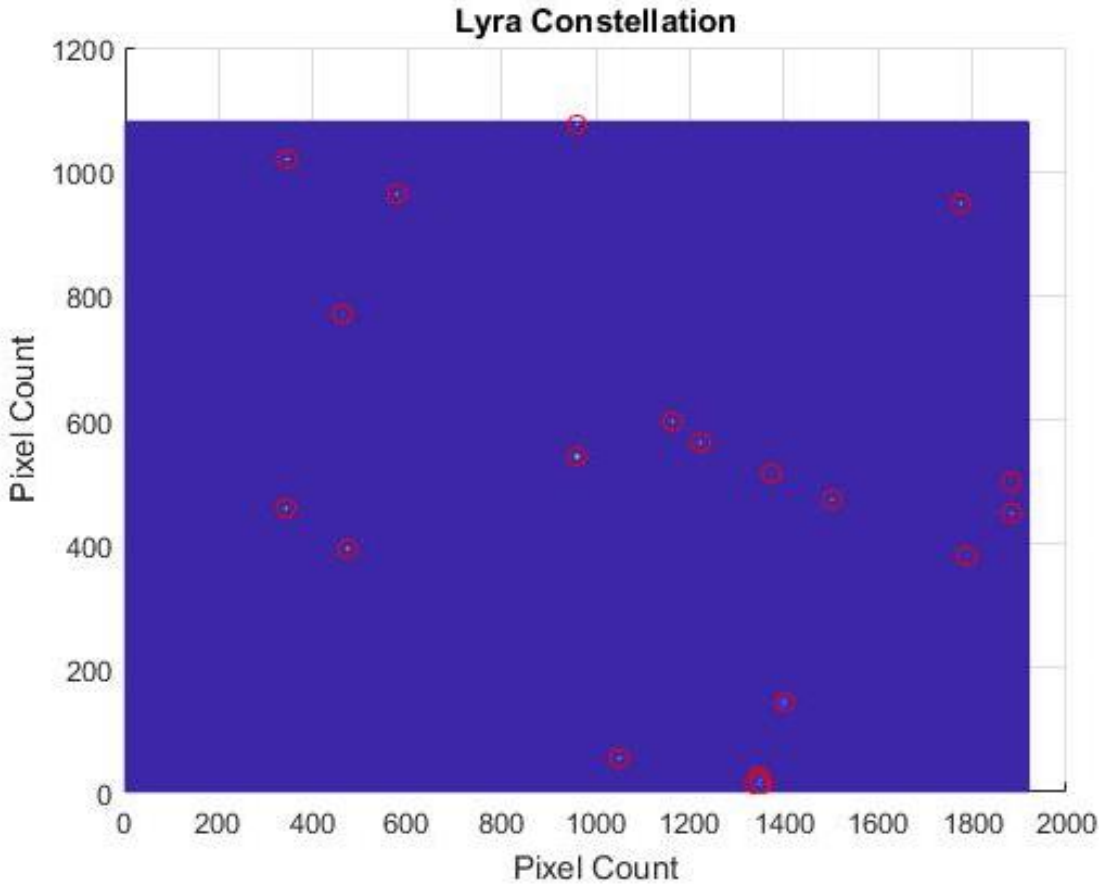


**Figure 31 Simulated Image with Centroid Locations**

### 6.1.2 Effect of Centroid Pixel Distortion on Identification Algorithm

In order to characterize the pixel error of the centroiding algorithm in relation to the accuracy of identification match, selected star clusters (groups of three stars that fell within the FOV) were used from the generated catalogue as the source data. Three test cases were examined by individually applying a deviation factor of 0.01% of a pixel to each set of values. The position of a star in the cluster was slightly shifted in a single orientation by adding or subtracting this deviation factor. Shifting the location of the star was accomplished in both directions until the identification process was no longer successful to produce the correct match between the star cluster and the catalogue. This shift along each axis provided the error boundary of the centroiding algorithm. The results of the 26437 star clusters are shown in Figure 32 Maximum Pixel Distortion X Axis, Figure 33 Maximum Pixel Distortion Y Axis and Figure 34 Maximum Pixel Distortion Z Axis with a table showing the mean value of each axis. The characterization of the centroiding algorithm to identification algorithm provides the average of the accuracy a star must be estimated to ensure a correct match in the subsequent algorithm. Examining the results of this section shows the X axis (longitude motion) is the least tolerant to pixel distortions followed by the Y (latitude motion) and Z axes, however all the tolerances are on the same scale.

**Table 6 Identification Algorithm Acceptance for Mean Value Pixel Distortion**

| Axis | Mean Value (Pixel Distortion) |
|---|---|
| X | 0.04% |
| Y | 0.05% |
| Z | 0.06% |

In summary, the simulation study suggests that any distortion more than 0.06% of the pixel size would not yield reasonable identification match results, as 50% uncertainty occurs once this distortion condition occurs.

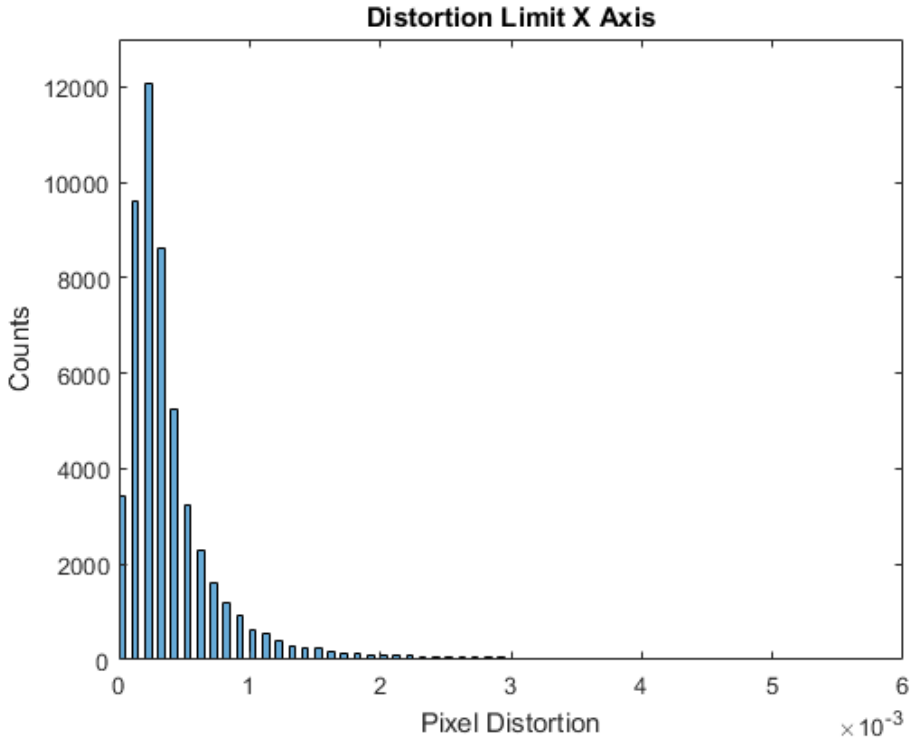


**Figure 32 Maximum Pixel Distortion X Axis**

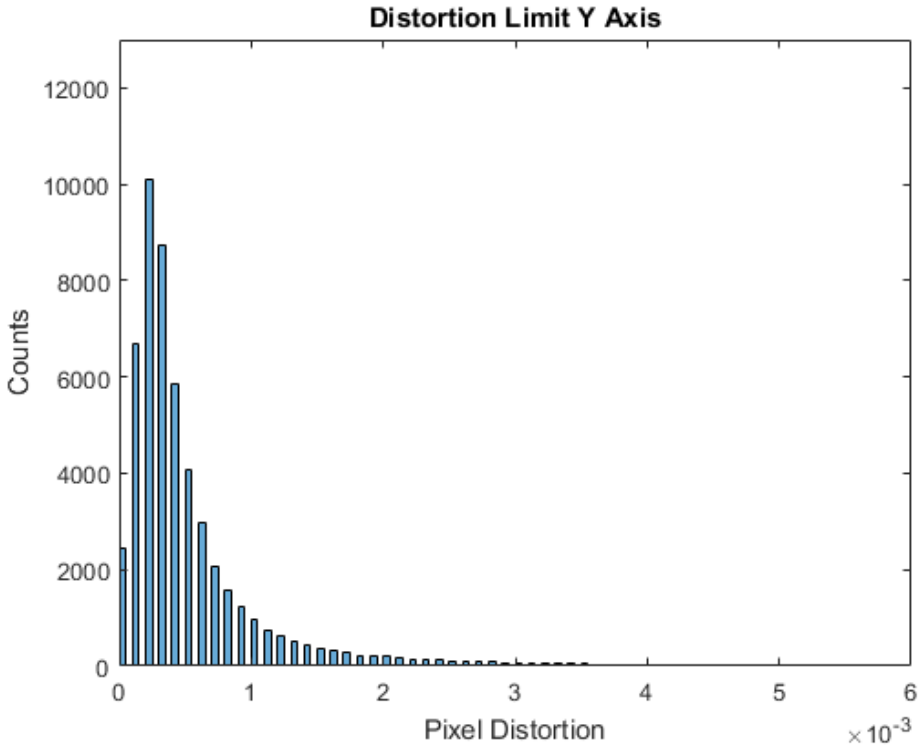


**Figure 33 Maximum Pixel Distortion Y Axis**

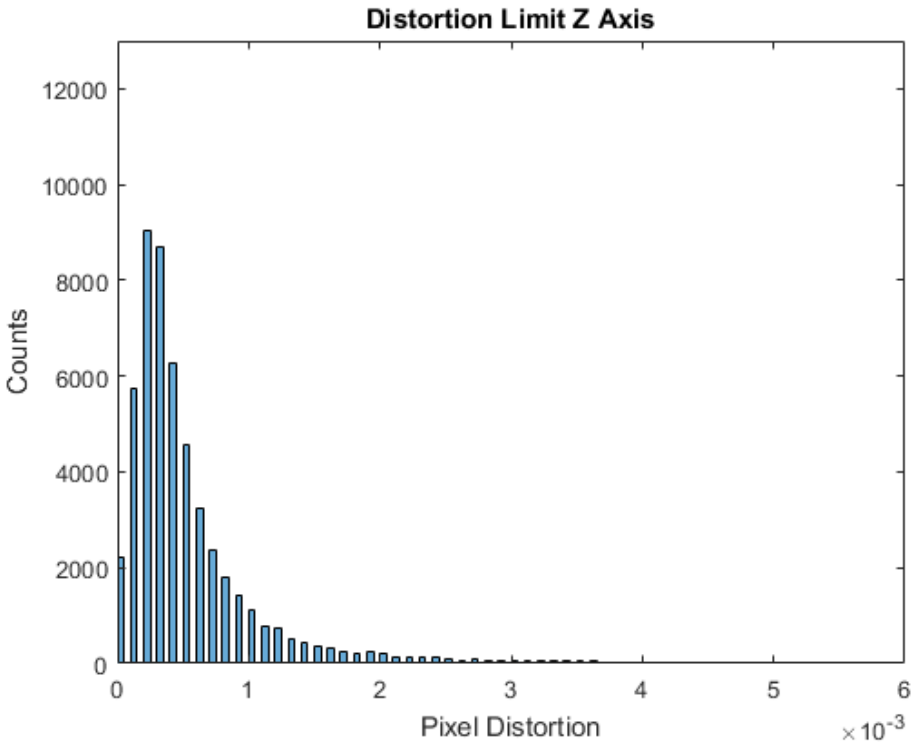


**Figure 34 Maximum Pixel Distortion Z Axis**

### 6.1.3 Effect of Centroid Pixel Distortion on Attitude Determination

A similar test was performed to characterize QUEST. As noted earlier, QUEST algorithm is known to have problems solving the attitude estimation for clusters of stars that have a tight proximity. Star clusters (groups of three stars that fell within the FOV) were once again used as the source data for the QUEST algorithm. Implementing the catalogue as the source data in this method bypasses the centroiding stage, allowing the identification algorithm to match the catalogue source data with the catalogue itself. This implementation characterizes QUEST to determine the number of cluster stars in the catalogue that achieve a correct match. A correct match for QUEST is the assigned quaternions $q_0$ a value of approximately one and the rest of the quaternions ($q_1$, $q_2$ and $q_3$) a value of approximately zero. To further characterize the QUEST algorithm with the generated catalogue, data was collected to test if there was a potential correlation to these mismatches and a clusters location on the celestial sphere. This was

accomplished at the same time as the original task of determining if QUEST would produce a correct quaternion match between data sets. The latitude and longitude of stars were saved and the locations were plotted to determine a correlation. The resulting data produced a randomly scattered plot all over the celestial sphere indicating that the failed tests do not have an obvious correlation.

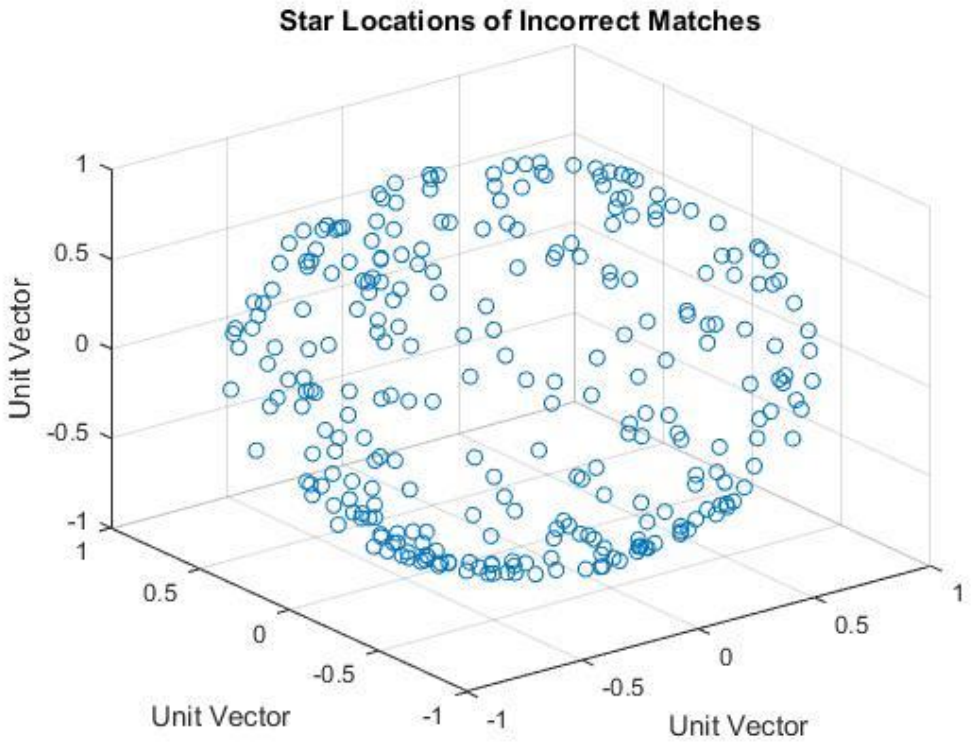


**Figure 35 Star Locations of Incorrectly Identified Stars**

The total of 26537 clusters was generated as study cases. From the total number of test cases, 25564 clusters yielded the desired quaternion (96.7%), while 873 did not achieve the desired result. The failed cases did not appear to have been caused by a specific regional effect as they were randomly scattered throughout the celestial sphere.

In order to determining the effectiveness of the entire star imager algorithm with added distortions, a test was implemented to gradually increase the pixel error. The input source data started with the catalogue and gradually increased the pixel distortion of a single star in the X axis. The distortion was increased in increments of 0.01% of a pixel until 1% of a pixel distortion was achieved. The information was then plotted on a log-log scale to demonstrate the algorithms functionality. The star imager algorithm drops below approximately 50% functionality once the distortions are larger than 0.08% of a pixel. However, the results also show that for several groups of stars the distortion of 1% is possible before the loss of attitude knowledge. This test shows the limitations of the system as the correct estimation of a star location is required to be within 0.04% of a pixel to achieve a successful attitude determination as approximately 75% of the catalogue can still achieve the desired result with this amount of distortion.

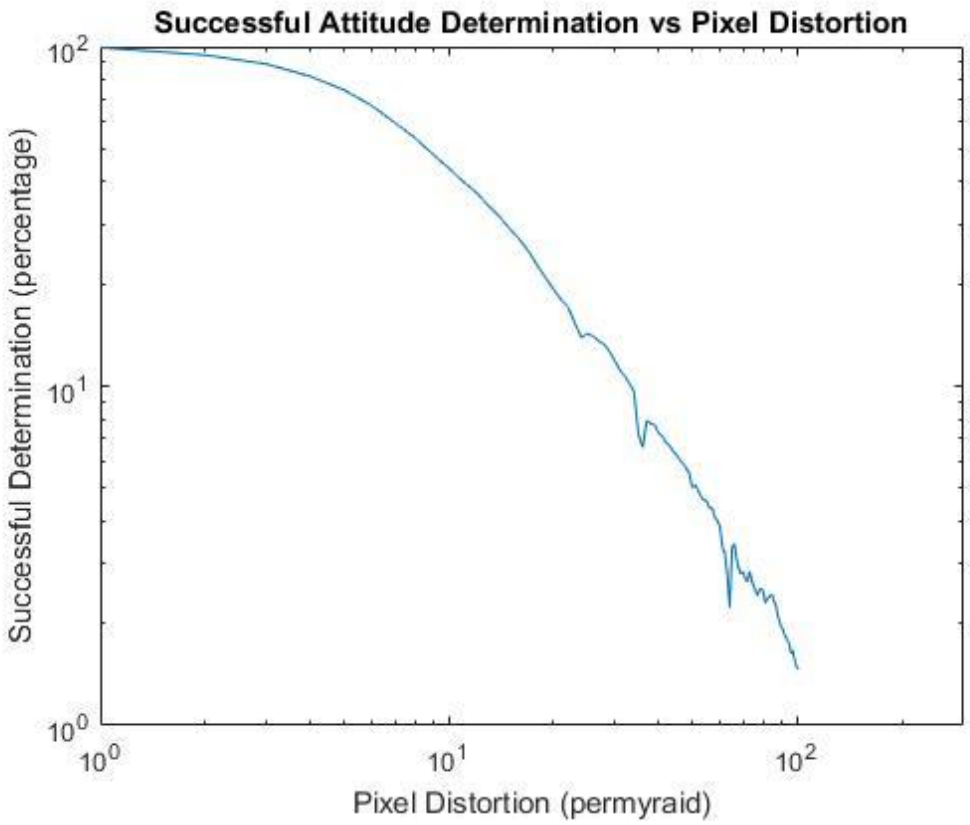


**Figure 36 Successful Attitude Determination versus Pixel Distortion in a Single Axis**

The tests on attitude determination (using QUEST algorithm) with the pixel distortion suggest that a high accuracy of the centroid algorithm (better than 0.08% pixel distortion) is required for the implemented identification algorithm to produce valid results. Therefore, these algorithms will likely only produce high accuracy attitude determination results on a consistent basis if the system includes optical components capable of an extremely high accuracy, which may increase the cost of the overall system and limit the use for smaller research groups.

## 6.2 Field Test Results

In order to demonstrate the hardware and software, two sets of data were collected from the field campaign at Algonquin Park, Ontario, Canada. With the use of dark sky maps (Lorenz, 2006) and (weather forecasting) cloud condition websites (Rahill, 2016), the location of

Algonquin was decided for its dark sky with minimal light pollution and ease of access. Figure 37 Field Expedition Dark Sky Chart (Lorenz, 2006) shows the dark sky map of the area around Algonquin as well as the site locations where field images were gathered.

These field sites were selected for two main reasons. First, the quality of images the camera system can produces outside the laboratory setting were evaluated. The ideal test would be a space flight with the camera payload to avoid any interference from the atmosphere, weather conditions and environmental effects (temperature, for example). However, given the scope of this project, the field test was considered an alternative only to examine the feasibility, not necessarily to evaluate the characteristics of spaceborne star imager. The conditions at Algonquin tested the quality of the images to a high degree as the system performs with expectational results within the atmosphere and with the potential of unforeseen weather conditions. With the atmosphere, mostly clear with minimal light pollution at Algonquin the increased path length (from the star imager located on Earth as compared to in orbit) through the atmosphere will cause distortions to the star light that enters the camera optics. The second goal of the field work was to gather images that would allow for testing of the software implementation being constructed for the star imager. Testing beyond the laboratory is an important aspect as the camera images will differ from those generated in the lab, such as the added atmospheric conditions.

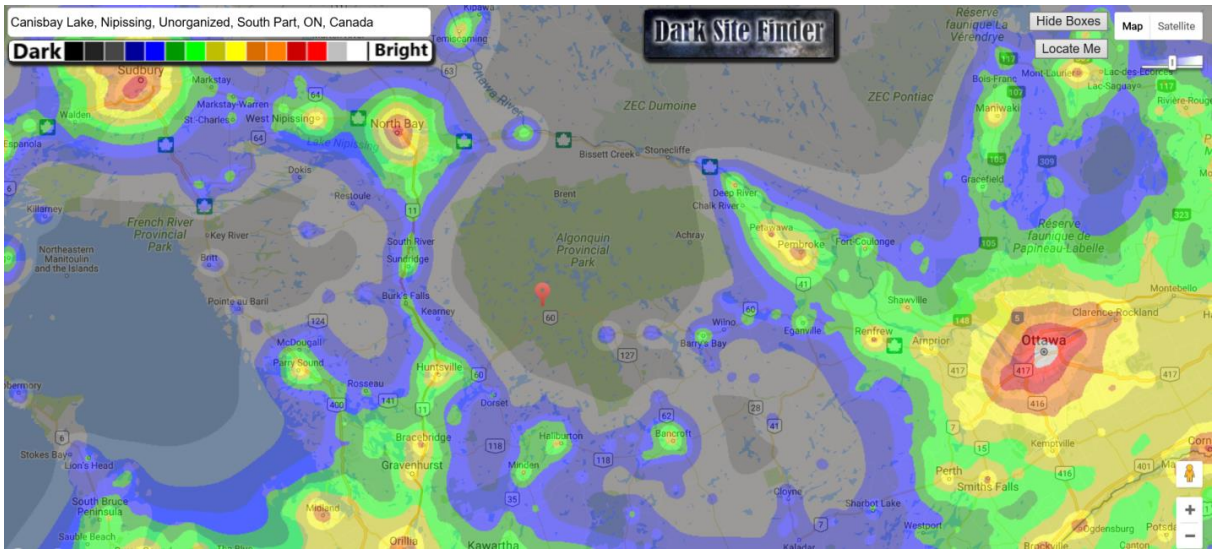


**Figure 37 Field Expedition Dark Sky Chart (Lorenz, 2006)**

### 6.2.1 Star Image Captured at Field Site: Brent Lake, Algonquin Park, Canada

Multiple night sky images were captured at Brent Lake but due to the difficulty of identifying stars amid noise present in the images prior to post-processing (in the field), only one image with a sufficient number of expected stars was obtained.

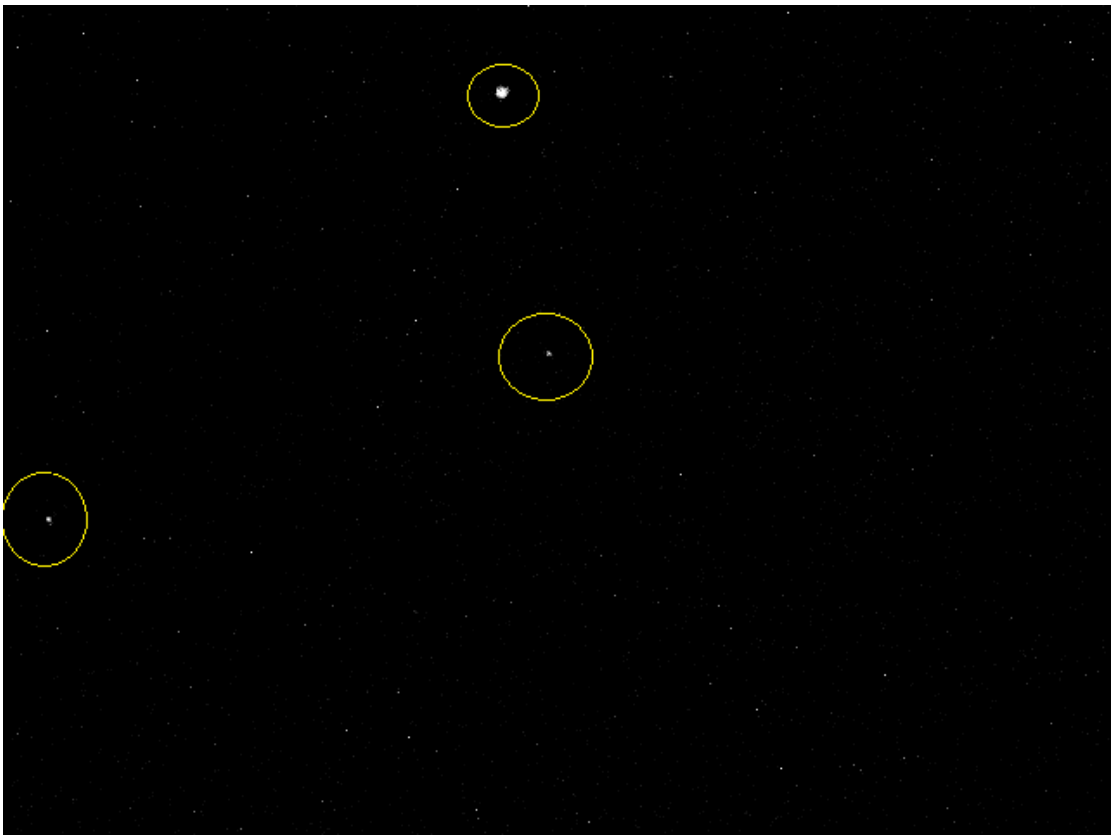

**Figure 38 Algonquin July 2015 (Brent Lake)**

During the field expedition, a star image was obtained by increasing the gain settings on the CMOS camera to the maximum setting because the apparent stars' brightness intensities were too low to be observed with unadjusted gain settings (Irvin, 2014). However, this also increased the noise floor in the images, predominantly due to an increase in dark current. The increased gain factor increases the apparent brightness of dim stars' that are marginally brighter than the noise floor to a detectable level. This also increases the brightness of stars that are much brighter than the noise floor to a level that these stars are now saturating the pixels. This amplification of the pixels' signal distorts the relative apparent magnitude of the stars as multiple stars will become saturated while dimmer stars are not. The use of this technique was possible due to the star imager algorithm not requiring the magnitude of the stars to solve the attitude determination problem. In order to distinguish stars' in the images the removal of the background noise is

required. The removal of noise is accomplished by subtracting a dark current image with the same increased gain setting resulting in Figure 38 Algonquin July 2015 (Brent Lake). There are three areas of signal that can be classified as possible stars in this image. The camera was pointed at the star Vega which is likely the largest cluster of pixels in the image. However, the limitation of this method is that if the floor noise level is not perfectly subtracted from the captured image, "false stars" may appear in the image that are not due to actual stars but due to remaining noise. In this case the noise floor was estimated using a single dark image. This is not an accurate method to determine the estimated noise floor and the most accurate method was demonstrated in chapter 5 DSNU calibration. This image cannot therefore be used to definitively validate the attitude determination algorithm because it is uncertain whether all the "stars" used are real.

**Table 7 Field Expedition Algorithm Determined Stars**

| Constellation (Expected) | Lyra | Constellation (Pre-Calibration) | Hercules | Constellation (Post-Calibration) | Perseus |
|---|---|---|---|---|---|
| Star 1 Identification | 7001 | Star 1 Identification | 6406 | Star 1 Identification | 1017 |
| Star 2 Identification | 7106 | Star 2 Identification | 6410 | Star 2 Identification | 1203 |
| Star 3 Identification | 7178 | Star 3 Identification | 6623 | Star 3 Identification | 1708 |

However, if the image contains the star Vega as expected, then the quadrant determined by the identification algorithm pre-calibration matches well with the expected quadrant Table 7 Field Expedition Algorithm Determined Stars. This gives confidence that the stars used in the attitude determination algorithm were likely stars and not due to excess noise post-subtraction. However, once calibration values were applied to the raw image the determined stars were predicted to a quadrant of the sky far from our intended target. The lack of agreement between the true pointing direction and the corrected attitude determination result could be due to errors in the correction,

"false" stars in the original image, or a combination of both. Further validation of the star imager algorithm is required though more images with higher quality (reduced noise) to properly test the performance.

### 6.2.2 Star Image Captured at Field Site: Cansby Lake, Algonquin Park, Canada

Although there were fewer technical issues during this field campaign compared to the previous campaign and it was generally apparent when stars were present in the image, cloud cover conditions only allowed one clear-sky image to be captured.

**Figure 39 Algonquin July 2016 (Cansby Lake)**

During a second field expedition to Algonquin another star image was capture using Vega again as the targeted star. The gain function was decreased compared to the first expedition and set to the value that was used in the calibration procedure to ensure minimal noise was amplified. The

image has a single star in the FOV with a well-defined PSF Figure 40 Algonquin Park 2016 PSF. This image demonstrates the functionality of the hardware to acquire star images in the field with a high signal to noise ratio.

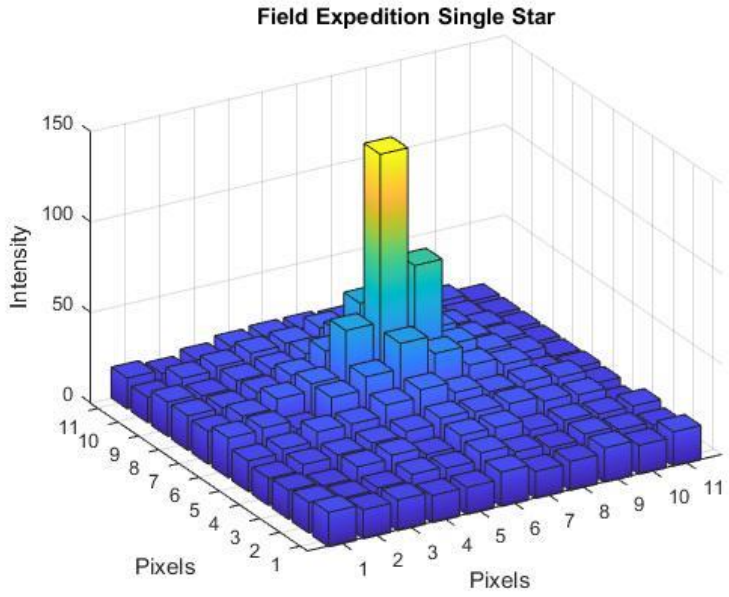


**Figure 40 Algonquin Park 2016 PSF**

## 6.3 Estimated Accuracy of the images from the field work

An estimation in the accuracy of a star imagers pointing direction and associated error is often estimated based on the cameras physical parameters such as the array size of the sensor, the minimum detectable magnitude, and the FOV of the optical system. The average number of stars visible in the FOV is calculated using the size of the catalogue and the cosine of the FOV. The estimated point direction and its associated error can then be calculated using the average number of stars that appear in an image.

$$N_{FOV} = \frac{N_{Cat.} - N_{Cat.} * \cos(\frac{FOV}{2})}{2}$$

$$PD_{error} = \frac{FOV * E_{Centroid}}{N_{Pixels} * \sqrt{N_{FOV}}}$$

$$PD_{estimated} = \frac{E_{Centroid}}{\sqrt{N_{FOV}}}$$

Where $N_{cat}$ is the number of stars in the catalogue dependent on the magnitude limit the sensor can detect. FOV is the field of view of the designed system, typically less than 40°. $E_{centroi}$ is the average hyperacuity of the centroiding accuracy. $N_{Pixels}$ is the number of pixels across the focal plane and is dependent on resolution of the sensor implemented. Lastly, $N_{FOV}$ is the number of stars visible in the FOV. This estimation of the star imager is theoretical as the detecting magnitude of the imager is an unknown value, this theoretical estimation therefore provides the upper limit estimation of the possible performance that star imager.

$$N_{FOV} = \frac{170 - 170 * \cos(\frac{30.8}{2})}{2} = 3$$

$$PD_{error} = \frac{30.8 * 0.1\ pixel}{560 * \sqrt{3}} = 0.00318$$

$$PD_{estimated} = \frac{0.1\ pixel}{\sqrt{3}} = 0.0577$$

The results from the above equations show that the hardware used for this research (on the assumptions magnitude three stars is the detection limit) can obtain three stars in the FOV. Therefore, the equations above estimate the pointing direction to 0.0577 degrees or 3.23 arcmin with an estimated error of plus or minus 0.00318 degrees or 0.188 arcmin. This theoretical calculation demonstrates the performance of the star imager, to properly evaluate the results field images with multiple stars are required to demonstrate a fully functional star imager.

# Chapter Seven: Conclusion and Future Work

## 7.1 Conclusion

Until recently the use of star imagers for attitude determination on CubeSats has been limited by star imagers' complicated design, size and associated expensive infrastructure requirements. Therefore, while star images provide the most accurate determination of attitude, other methods have traditionally been used to achieve attitude determination. Accurate attitude knowledge is essential for advanced scientific missions to ensure accurate pointing is obtained. Since star imagers provide high accuracy, it would be advantageous to the field of satellite measurements to be able to effectively utilise them on CubeSats. While advancing technologies and algorithms are gradually decreasing the costs associated with these systems, the commercially available systems are still very expensive. In this study, we examined the functionality of a simple, low-cost commercial camera (previously referred to as COTS system) to provide attitude knowledge in place of relying on dedicated, high-power star imager. If we demonstrate that a commercial CMOS camera (often onboard CubeSats for imaging purposes other than star tracking or star identification) is suitable to provide attitude information with limited accuracy and availability, the proposed approach can be implemented on projects accessible to university research groups and for relatively quick and inexpensive deployments for research organizations and industry.

The primary research objective of this thesis was, therefore, to evaluate the feasibility of a COTS CMOS star imager to provide attitude knowledge for a Nanosatellite. The thesis focused on the selection and implementation of a star imager algorithm. The research objectives were to (1) identify the methods required to develop the star imager algorithm, (2) characterize the

performance of the algorithm and (3) characterize the overall performance of the COTS CMOS camera.

These research objectives were achieved through: development of a star imager algorithm and implementing algorithms that are appropriate for CubeSat performance requirements; calibration of a typical CMOS camera hardware to determine the lens and sensor parameters; and characterization of the star-camera algorithm though a series of simulations, in-lab and field tests.

Three algorithms were considered: centroiding, star identification, and attitude determination. For each sub-algorithm, exisiting methods were evaluated and the optimal method was implemented based on the typical requirements of CubeSats and the associated data that was provided from the hardware. The subroutines in the following paragraphs constitute the architecture of the star imager algorithm to fulfill the primary objective of this research.

The first centroiding algorithm that was considered is the thresholding method, which was designed to determine the difference between pixels that have a high enough photon count to be considered a star compared to the background noise of the camera. As the noise floor remains relatively constant from image to image, the use of a general thresholding method over an entire image allows for a single calculation of the background noise and reduces the amount of computation time for this subroutine. Alternatively, the COM method is one of the fastest and most computationally efficient methods for estimating the location of stars. This method does have the disadvantage of a high sensitivity towards large amounts of background noise (Auer and Altena, 1978). The centroiding algorithms accuracy can be increased with the intentional defocusing of the optics system to a 5 by 5 or 7 by 7 PSF (Delabie, 2016), however this

intentional defocusing decreases the signal to noise ratio. Due to the limitations of COTS components used in this research, the background noise over time should increase as the components are not made of "space grade" materials and will degrade faster than high quality components. As the life span of a nanosatellite is often only a few years the trade-off between a fast and efficient algorithm outweighs the limitation imposed by the potential of degrading components.

The BSC was selected as the catalogue for the identification algorithm due to the limitations of the optical system that cannot detect stars below the visual magnitude of the catalogue. The BSC is a small catalogue with 9110 objects with 9096 of these being stars that are visible to the human eye. The field expeditions from the previous research and this research have demonstrated the effectiveness of the system to observe stars within the magnitude of the selected catalogue thereby not requiring the implementation of a larger catalogue. An increased focal ratio on the lens used in this research was implemented to increase the number of photons on the detector so that the camera can observe the maximum number of stars in this catalogue.

For star identification, grid, voting and polygon techniques were considered based on their simplicity and computationally efficient design. The polygon identification algorithm was selected and the area and polar moment method was implemented for this research because this method works well for the limited number of stars that the camera system can observe. It also performs the operation of comparing the image vectors to the catalogue values effectively as most algorithms require the use of a fourth star. The area and polar moment methods works by using the unit vectors of three stars in the FOV, using these stars the sides of a triangle are

calculated. From this triangle, the area and moment values are determined and used as the search criteria to be compared to the star catalogue.

Lastly, the QUEST method was chosen for the attitude determination algorithm because of its ease of implementation, relative robustness and high performance, which match the needs of most CubeSats.

Star imager calibration tests were conducted in order to characterize the camera system and to enhance the overall performance by accurately correcting measurement data. The majority of the calibrations were accomplished with the used of the publicly available Calibration Toolbox for MATLAB. These tests include a spatial pattern test, which used a checker board pattern to determine distortions introduced into the system from the lens and sensor. FPN was determined using a flat field illumination test performed with a uniformly illuminated screen. The dark noise test was performed with no illumination to quantify the number of hot pixels. To determine the response of the system from an impulse point source the PSF test was performed. The results of these tests indicated that the camera performance was within the expected range for a COTS system but some distortions are caused from incorrect alignment of the lens. This distortion can be fixed by a calibration technique to image the lens as it is mounted to the senor body. The sensor had a uniform response under the flat field, however there were several hot pixels determined from the dark response tests. The PSF tests fit within the expectations of an isotropic distribution near the middle of the sensor and non-isotropic distribution when the test was performed closer to the edges.

Characterization of the algorithm and camera performance was accomplished using simulated star images and dark sky images obtained during field expeditions. In the ideal case

(no noise) the star imager algorithm estimates attitude correctly approaching 100% of the time. The characterization test results indicate that for this system a small error (0.04%) in the pixel estimation by the centroiding algorithm results in a decrease to 75% successful match retrieval between the star image and the catalogue. However, once the error increases to 0.08% of a pixel by the centroiding algorithm, the attitude determination algorithm quickly losses its ability to be a reliable system as 50% of the cases will not produce an accurate result.

The evaluation of the algorithm was limited by the small number of images obtained during field campaigns due to weather conditions preventing unobstructed views of the night sky. Also, the brightness of the visible stars was very low, which prevented an image where stars could be reliably identified. Even under ideal atmospheric conditions, camera images obtained at the surface are limited by atmospheric attenuations of light and light pollution and cause stars to appear dimmer then they would be seen from space. Therefore, these images are not ideal for characterization of the star imager but the results of the quadrant matching suggest that the performance pre-calibration was acceptable given the limitations.

## 7.2 Future Work

The importance and use of nanosatellites will continue to grow rapidly in the future and attitude determination systems must improve in accuracy, cost effectiveness and ease of implementation in order to keep pace with the scientific needs.

Future work to improve and build upon this work includes determining the detectable magnitude of the star imager. Due to the small number of images that had a number of limitations collected in the field, the minimum brightness of the system is able to detect is unknown. Performing in-lab tests with a calibrated light source or obtaining more clear sky star

images can provide this information. Ideally, sky images should be obtained with a variety of number of visible stars and with stars of varying brightness in order to examine the camera capabilities under these range of conditions. These tests in-lab and with more and better quality clear dark sky images will help further evaluate the capability of the COTS components of observing enough stars in the sky at a single frame to provide attitude knowledge in a timely manner.

The star imager algorithm performs the LIS case for each attitude determination. The LIS case is designed for a star camera to determine its initial attitude and then uses a tracking method to maintain the attitude knowledge thereafter. To develop the system into a star tracker the implementation of a tracking algorithm is required to increase the efficiency of the system. Tracking methods are computationally more efficient than performing the LIS case for each measurement.

The implementation of a faster search method should also be implemented to increase performance in the identification algorithm. The identification algorithm searches the catalogue in a linear method from beginning to end. To decrease the computational, time the implementation of the K-vector or another form of breadth first search algorithm is required. This type of search method was not implemented into the existing research as an increase computational method will not change the results of the search algorithm and only increase the speed of the results are obtained.

The field site and campaign structure should be redesigned to incorporate a higher altitude location to reduce the atmospheric effects that hindered much of the field work during this research. This can be addressed by either moving the field site to the top of a mountain or

through the implementation of a balloon. A balloon system would require a mounting system for the entire hardware used to collect data, which is more complex to implement than a field site at a higher altitude, however, the travel cost to a higher altitude location could outweigh the design complications.

The study of characterizing the algorithm should be continued through the study of image smearing. The effects of the satellite orbiting will result in images that have elongated tails on the imaged stars. These centroiding algorithm must determine the middle of the star at the end of the tail ensuring that part of the signal from the tail is used in the centroiding to skew the estimated location. In order to perform the study the current tripod mount would have to be changed to a gimbal system that can control the rate of rotation.

The algorithm was designed for COTS components that were of low quality in order to examine if extremely low cost components could still obtain the required attitude determination accuracy. Using higher quality components will quickly increase the performance of the system. Future work is required to examine at what increased cost the performance significantly increases since a balance between cost and acceptable performance needs to be identified. If this is achieved, these new relatively low cost attitude determination systems could significantly enhance the quality of the scientific results of CubeSats at a more accessible cost, allowing more research groups to achieve their scientific objectives in shorter periods of time.

# References


Anon: Payload Orbital Delivery System (PODS) User's Guide, 2017.

Aretskin-Hariton, E. and Swank, A. J.: Star Tracker Performance Estimate with IMU, in AIAA Guidance, Navigation, and Control Conference, p. 0334. [online] Available from: https://arc.aiaa.org/doi/pdfplus/10.2514/6.2015-0334 (Accessed 3 September 2017), 2015.

Auer, L. H. and Altena, W. F.: Digital Image Centering. II, Astron. J., 83(5) [online] Available from: http://articles.adsabs.harvard.edu/cgi-bin/nph-iarticle_query?bibcode=1978AJ.....83..531A&db_key=AST&page_ind=0&data_type=GIF&type=SCREEN_VIEW&classic=YES (Accessed 4 September 2017), 1978.

Birnbaum, M. M., Salomon, P. M. and Uematsu, R.: Voyager Spacecraft 31 Canopus Star Tracker S/N 205, [online] Available from: https://oce.jpl.nasa.gov/mib/VOY-1.pdf (Accessed 3 September 2017), 1980.

Black: A Passive System for Determining the Attitude of a Satellite, Defense Technical Information Center., 1963.

Blue Canyon Technologies: DataSheet TS Nano Star Tracker, n.d.

Bouguet, J. Y.: Camera Calibration Toolbox for Matlab, Camera Calibration Toolbox Matlab [online] Available from: http://www.vision.caltech.edu/bouguetj/calib_doc/ (Accessed 4 September 2017), 2015.

Browse Software Development Team: HIPPARCOS - Hipparcos Main Catalog, [online] Available from: https://heasarc.gsfc.nasa.gov/W3Browse/all/hipparcos.html (Accessed 4 September 2017), 2012.

Calizo, I. G.: Reset Noise in CMOS Image Snesors, Master of Science, San Jose State University, San Jose, August. [online] Available from:

http://scholarworks.sjsu.edu/cgi/viewcontent.cgi?article=3742&context=etd_theses (Accessed 3 September 2017), 2005.

Carroll, K., Rucinski, S. and Zee, R.: Arc-minute nanosatellite attitude control: Enabling technology for the BRITE stellar photometry mission, [online] Available from: http://digitalcommons.usu.edu/smallsat/2004/All2004/24/ (Accessed 28 August 2017), 2004.

Catrysse, P. B., Liu, X. and El Gamal, A.: QE reduction due to pixel vignetting in CMOS image sensors, in Proc. SPIE, vol. 3965, pp. 420–430. [online] Available from: https://pdfs.semanticscholar.org/7213/57765efeb55f4aadd0a4ac0897ab9a94ad16.pdf (Accessed 4 September 2017), 2000.

Cheng, Y. and Shuster, M. D.: Improvement to the Implementation of the QUEST Algorithm, J. Guid. Control Dyn., 37(1), 301–305, doi:10.2514/1.62549, 2014.

Cole, C. L. and Crassidis, J. L.: Fast star-pattern recognition using planar triangles, J. Guid. Control Dyn., 29(1), 64–71, 2006.

Delabie, T.: Star Tracker Algorithms and a Low-Cost Attitude Determination and Control System for Space Missions, [online] Available from: https://lirias.kuleuven.be/handle/123456789/514285 (Accessed 4 September 2017), 2016.

Delabie, T., De Schutter, J. and Vandenbussche, B.: An accurate and efficient gaussian fit centroiding algorithm for star trackers, J. Astronaut. Sci., 61(1), 60–84, 2014.

Diaz, K. D.: Performance Analysis Of A Fixed Point Star Tracker Algorithm, San Luis Obispo: California Polytechnic State University. [online] Available from: http://www.crn2.inpe.br/conasat1/projetos_cubesat/projetos/CP1%20-%20California%20Polytechnic%20Institute%20-%20USA/CP1%20-%20ADCS%20-%20Analisys%20of%20a%20Fixed%20Point%20Star%20Tracker%20Algorithm.pdf (Accessed 27 September 2017), 2006.

Doncaster, B. and Shulman, J.: Nano/Microsatellite Market Forcast, 2016.

Duarte, R. O., Martins-Filho, L. S. and Kuga, H. K.: PERFORMANCE COMPARISON OF ATTITUDE DETERMINATION ALGORITHMS DEVELOPED TO RUN IN A

MICROPROCESSOR ENVIRONMENT, [online] Available from: http://www.abcm.org.br/anais/cobem/2009/pdf/COB09-0773.pdf (Accessed 28 August 2017), 2009.

Dzamba, T.: Improving the measurement quality of small satellite star trackers, Ph. D. dissertation, Ryerson University, Department of Aerospace Engineering. [online] Available from: http://digital.library.ryerson.ca/islandora/object/RULA:1977/datastream/OBJ/download/Improving_the_Measurement_Quality_of_Small_Satellite_Star_Trackers.pdf (Accessed 3 September 2017), 2013.

Erlank, A. O.: Development of CubeStar: a CubeSat-compatible star tracker, Stellenbosch: Stellenbosch University. [online] Available from: http://scholar.sun.ac.za/handle/10019.1/85746 (Accessed 28 August 2017), 2013.

Fischer, W., Balagurin, O., Kayai, H. and Wojtkowiak, H.: Hardware software solutions for miniature star sensors, German Society for Aeronautics and Astronautics, Germany. [online] Available from: http://www.dglr.de/publikationen/2014/340071.pdf (Accessed 3 September 2017), 2014.

Hasinoff, S. W.: Photon, poisson noise, in Computer Vision, pp. 608–610, Springer. [online] Available from: http://link.springer.com/10.1007%2F978-0-387-31439-6_482 (Accessed 3 September 2017), 2014.

Hille, K.: NASA Engineer Advances New Daytime Star Tracker, NASA [online] Available from: http://www.nasa.gov/content/goddard/nasa-engineer-advances-new-daytime-star-tracker (Accessed 3 September 2017), 2015.

Hornsey, R. I.: Noise in Image Sensors, [online] Available from: https://www.eecs.tu-berlin.de/fileadmin/fg144/Courses/10WS/pdci/talks/noise_sensors.pdf (Accessed 4 September 2017), 2008.

Huffman, K. M.: Designing Star Trackers to Meet Micro-Satellite Requirements, Master of Science in Aeronautics and Astronautics, Massachusetts Insitute of Technologhy, 26 May., 2006.

Irvin, P.: CMOS Imager for Nanosatellite Applications, York University, Toronto, Ontario., 2014.

Kandiyil, R.: Attitude Determination Software for a Star Sensor, Lulea University of Technology, Germany., 2009.

Kennedy, R.: Fitting a Gaussian (normal distribution) curve to a histogram in Tableau, Inf. Lab [online] Available from: https://www.theinformationlab.co.uk/2013/11/04/fitting-a-gaussian-normal-distribution-curve-to-a-histogram-in-tableau/ (Accessed 28 September 2017), 2013.

Kerimovich, A. M.: DataSheet Star Tracker AZDK-1, n.d.

Knight, S., Moschou, S. and Sorell, M.: Analysis of Sensor Photo Response Non-Uniformity in RAW Images., in e-Forensics, pp. 130–141, Springer. [online] Available from: http://link.springer.com/content/pdf/10.1007/978-3-642-02312-5.pdf#page=140 (Accessed 4 September 2017), 2009.

Koene, B.: How to use Flat Field Correction in practice?, [online] Available from: http://info.adimec.com/blogposts/how-to-use-flat-field-correction-in-practice (Accessed 4 September 2017), 2016.

Lasker, B. M., Sturch, C. R., McLean, B. J. and Russell, J. L.: THE GUIDE STAR CATALOG. I. ASTRONOMICAL FOUNDATIONS AND IMAGE PROCESSING, Astron. J., 99(6), 6, 1990.

Lee, S., Ortiz, G. G. and Alexander, J. W.: Star tracker-based acquisition, tracking, and pointing technology for deep-space optical communications, Interplanet. Netw. Prog. Rep., 42(161), 42–161, 2005.

Liebe, C. C.: Star trackers for attitude determination, IEEE Aerosp. Electron. Syst. Mag., 10(6), 10–16, doi:10.1109/62.387971, 1995.

Lorenz, D.: DarkSiteFinder.com - Light Pollution Map, [online] Available from: http://darksitefinder.com/maps/world.html (Accessed 4 September 2017), 2006.

Luo, L., Xu, L. and Zhang, H.: An Autonomous Star Identification Algorithm Based on One-Dimensional Vector Pattern for Star Sensors, Sensors, 15(7), 16412–16429, doi:10.3390/s150716412, 2015.

Mahajan, V. N.: Optical Imaging and Aberrations: Ray geometrical optics, SPIE Press., 1998.

Malacara, D., Malacara, Z. and Malacara, D.: Handbook of optical design, 2nd ed., Marcel Dekker, New York., 2004.

Markley, F. L. and Mortari, D.: How to Estimate Attitude from Vector Observations, Am. Astron. Soc. [online] Available from: http://malcolmdshuster.com/FC_MarkleyMortari_Girdwood_1999_AAS.pdf (Accessed 4 September 2017), 2000.

McBryde, C. R. and Lightsey, E. G.: A star tracker design for CubeSats, MASTER OF SCIENCE IN ENGINEERING, UNIVERSITY OF TEXAS, AUSTIN, May. [online] Available from: http://ieeexplore.ieee.org/abstract/document/6187242/ (Accessed 2 September 2017), 2012.

Mortari, D., Samaan, M. A., Bruccoleri, C. and Junkins, J. L.: The Pyramid Star Identification Technique, 1997.

NanoRacks, L. L. C.: NanoRacks CubeSat Deployer (NRCSD) Interface Control Document, 0.36 [online] Available from: http://nanoracks.com/wp-content/uploads/Current_edition_of_Interface_Document_for_NanoRacks_Smallsat_Customers.pdf (Accessed 2 September 2017), 2013.

Padgett, C. and Del Gado, K. K.: A Grid Algorithm for Autonomous Star Identification, IEEE Trans. Aerosp. Electron. Syst., 33 [online] Available from: https://trs.jpl.nasa.gov/bitstream/handle/2014/27621/96-1672.pdf?sequence=1&isAllowed=y (Accessed 4 September 2017), 1997.

Pignatelli, D.: Poly Picosatellite Orbital Deployer Mk. III Rev E. User Guide, 2014.

Porter, W. C., Kopp, B., Dunlap, J. C., Widenhorn, R. and Bodegom, E.: Dark current measurements in a CMOS imager, edited by M. M. Blouke and E. Bodegom, p. 68160C., 2008.

Rahill, A.: Clear Sky Chart, [online] Available from: http://www.cleardarksky.com/c/Blackfootkey.html?1 (Accessed 4 September 2017), 2016.

Sakakibara, M., Kawahito, S., Handoko, Q., Nakamura, N. and Satoh, H.: A CMOS Image Sensor with Gain-Adaptive Column Aplifiers, IEEE J. Solid-State Circuits, 40(5), 1147–1156, doi:10.1109/JSSC.2005.845969, 2005.

Sasian, J. M.: Introduction to aberrations in optical imaging systems, Cambridge University Press, Cambridge ; New York., 2013.

Sidi, M. J.: Spacecraft Dynamics and Control: A Practical Engineering Approach, Cambridge University Press., 2000.

Smith, W. J.: Modern optical engineering: the design of optical systems, 3rd ed., McGraw Hill, New York., 2000.

Spratling, B. B. and Mortari, D.: A Survey on Star Identification Algorithms, Algorithms, 2(1), 93–107, doi:10.3390/a2010093, 2009.

Sudhakaran, S.: The 15 Things to Look Out For in a Camera Lens (Part Two): More Lens Aberrations | Wolfcrow, [online] Available from: http://wolfcrow.com/blog/things-to-look-out-for-in-a-camera-lens-part-two-more-lens-aberrations/ (Accessed 4 September 2017), 2013.

Tian, H.: Noise Analysis in CMOS Image Sensors, Degree of doctor of philosophy, stanford university, August., 2000.

Toczek, T., Hamdi, F., Heyrman, B., Dubois, J., Miteran, J. and Ginhac, D.: Scene-based non-uniformity correction: From algorithm to implementation on a smart camera, J. Syst. Archit., 59(10), 833–846, doi:10.1016/j.sysarc.2013.05.017, 2013.

Wahba, G.: A Least Squares Estimate of Spacecraft Attitude, SIAM Rev., 7(3), 384–386, 1965.

Warren Jr., W. H.: Bright Star Catalogue, 5th Revised Ed., [online] Available from: http://cdsarc.u-strasbg.fr/viz-bin/Cat?V/50 (Accessed 4 September 2017), 1991.

Weng, J., Cohen, P., Herniou, M. and others: Camera calibration with distortion models and accuracy evaluation, IEEE Trans. Pattern Anal. Mach. Intell., 14(10), 965–980, 1992.

Wertz, J. R.: Spacecraft Attitude Determination and Control, Springer Science & Business Media., 2012.

Wertz, J. R. and Larson, W. J., Eds.: Space mission analysis and design, 3rd ed., Microcosm ; Kluwer, El Segundo, Calif. : Dordrecht ; Boston., 1999.

Xie, J., Tang, X., Jiang, W. and Fu, X.: An autonomous star identification algorithm based on the directed circularity pattern, star, 4, 5, 2012.

Zhang, Z.: Flexible camera calibration by viewing a plane from unknown orientations, in Computer Vision, 1999. The Proceedings of the Seventh IEEE International Conference on, vol. 1, pp. 666–673, Ieee. [online] Available from: http://ieeexplore.ieee.org/abstract/document/791289/ (Accessed 4 September 2017), 1999.